Sequential Star Formation in the Young SMC Region NGC 602: Insights from ALMA

Theo J. O'Neill[1] , Rémy Indebetouw[1,2] , Karin Sandstrom[3] , Alberto D. Bolatto[4] , Katherine E. Jameson[5] ,
Lynn R. Carlson[6], Molly K. Finn[1] , Margaret Meixner[7] , Elena Sabbi[8] , and Marta Sewiło[4,9,10]

[1] Department of Astronomy, University of Virginia, Charlottesville, VA 22904, USA; oneill@virginia.edu
[2] National Radio Astronomy Observatory, 520 Edgemont Road, Charlottesville, VA 22903, USA
[3] Center for Astrophysics and Space Sciences, Department of Physics, University of California, San Diego, 9500 Gilman Drive, La Jolla, CA 92093, USA
[4] Department of Astronomy, University of Maryland, College Park, MD 20742, USA
[5] CSIRO Space and Astronomy, ATNF, PO Box 1130, Bentley, WA 6102, Australia
[6] Experimental College, Tufts University, Medford, MA 02155, USA
[7] SOFIA Science Mission Operations/USRA, NASA Ames Research Center, Bldg. N232, M/S 232-12, P.O. Box 1, Moffett Field, CA 94035-0001, USA
[8] Space Telescope Science Institute, 3700 San Martin Drive, Baltimore, MD 21218, USA
[9] Exoplanets and Stellar Astrophysics Laboratory, NASA Goddard Space Flight Center, Greenbelt, MD 20771, USA
[10] Center for Research and Exploration in Space Science and Technology, NASA Goddard Space Flight Center, Greenbelt, MD 20771, USA

Abstract

NGC 602 is a young, low-metallicity star cluster in the "Wing" of the Small Magellanic Cloud. We reveal the recent evolutionary past of the cluster through analysis of high-resolution ($\sim$0.4 pc) Atacama Large Millimeter/ submillimeter Array observations of molecular gas in the associated H II region N90. We identify 110 molecular clumps ($R < 0.8$ pc) traced by CO emission, and study the relationship between the clumps and associated young stellar objects (YSOs) and pre-main-sequence (PMS) stars. The clumps have high virial parameters (typical $\alpha_{\rm vir} = 4$–11) and may retain signatures of a collision in the last $\lesssim$8 Myr between H I components of the adjacent supergiant shell SMC-SGS 1. We obtain a CO-bright-to-H$_2$ gas conversion factor of $X_{\rm CO,B} = (3.4 \pm 0.2) \times 10^{20}$ cm^{-2} (K km s^{-1})$^{-1}$, and correct observed clump properties for CO-dark H$_2$ gas to derive a total molecular gas mass in N90 of $16{,}600 \pm 2400\,M_\odot$. We derive a recent ($\lesssim$1 Myr) star formation rate of $130 \pm 30\,M_\odot$ Myr^{-1} with an efficiency of $8\% \pm 3\%$ assessed through comparing total YSO mass to total molecular gas mass. Very few significant radial trends exist between clump properties or PMS star ages and distance from NGC 602. We do not find evidence for a triggered star formation scenario among the youngest ($\lesssim$2 Myr) stellar generations, and instead conclude that a sequential star formation process in which NGC 602 did not directly cause recent star formation in the region is likely.

1. Introduction

The young open cluster NGC 602 and associated H II region N90 are cradled in the "Wing" of the Small Magellanic Cloud (SMC) by the supergiant shell SMC-SGS 1 (hereafter SGS 1; Meaburn 1980; shown in Figure 1(a)). The SMC is an ideal location to study the effects of environment on the progression of star formation: it is a low-metallicity ($Z \sim 1/5\,Z_\odot$; Russell & Dopita 1992; Lee et al. 2005) and low gas surface density environment ($N \sim (2$–$8) \times 10^{21}$ cm^{-2}; Leroy et al. 2007; Welty et al. 2012), and is located at a distance of only $\sim$60.6 kpc (Hilditch et al. 2005). Under these conditions, the relationship between star-forming gas and commonly used observables like CO line emission is expected to depart from behaviors found at higher metallicities and densities. Molecular clouds experience significant photodissociation in gas with little dust (Gordon et al. 2011) and enhanced interstellar radiation fields (Madden et al. 2006; Gordon et al. 2008; Sandstrom et al. 2010); the fraction of H$_2$ that is CO-dark also increases with decreasing metallicity (Wolfire et al. 2010; Glover & Mac Low 2011; Szűcs et al. 2016).

The Wing marks the transition between the comparatively molecule-rich inner area of the SMC and the H I-dominated outer region leading to the Magellanic Bridge, which possesses even lower surface densities and metallicities than the main body of the SMC (Rolleston et al. 1999; Lehner et al. 2008; Gordon et al. 2009; Welty et al. 2012). NGC 602 and N90 have been extensively studied historically (e.g., Henize 1956; Westerlund 1964; Hodge 1983; Hutchings et al. 1991), and renewed interest in recent years has resulted in the region being remarkably well-characterized on a variety of spatial scales through a large range of wavelength regimes. When considered with its isolated location within the diffuse Wing, NGC 602/ N90 presents a valuable opportunity for tests of star formation theory under dramatically different conditions from the solar neighborhood.

The rate of star formation in the Wing has been increasing over the last 0.2 Gyr (Rubele et al. 2015, 2018), especially in the area surrounding N90 and the adjacent $\sim$500 pc diameter SGS 1 shell (Figure 1(a)). Ramachandran et al. (2019) performed a spectroscopic investigation of OB stars within SGS 1 and suggested that massive star formation has been ongoing over the past 100 Myr, including an extended star formation event between 30 and 40 Myr ago. Fulmer et al. (2020) extended this work using near-UV and optical photometry and observed no radial gradient in stellar ages
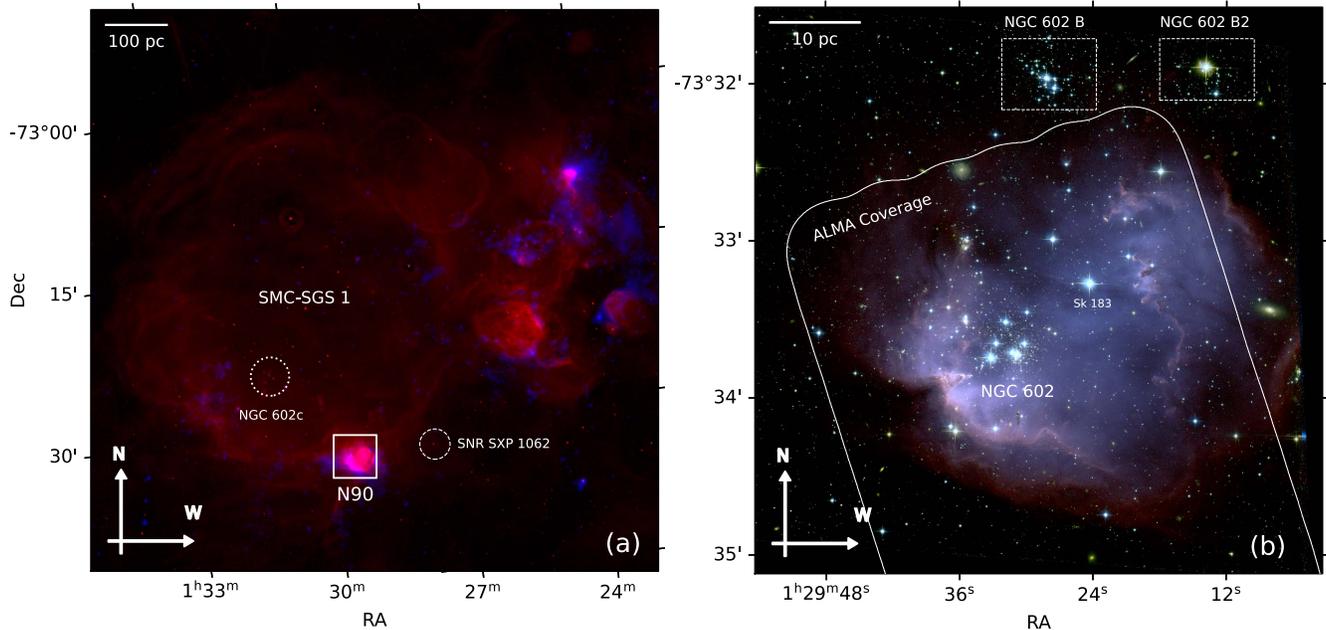
Figure 1. (a) Image of the supergiant shell SMC-SGS 1 in the SMC Wing. [R, B] = [Magellanic Cloud Emission-Line Survey Hα image, Herschel SPIRE 250 μm image]. The extent of the Hubble Space Telescope (HST) image of N90 shown in (b) is outlined with a white square. Supernova remnant (SNR) SXP 1062 is outlined with a white dashed circle, and the cluster NGC 602 c is marked with a white dotted circle. (b) HST Advanced Camera for Surveys (ACS) image of N90. [R, G, B] = [Hα + F814W, F555W + F814W, F555W]. The central cluster NGC 602 is labeled, and the extent of the Atacama Large Millimeter/submillimeter Array (ALMA) 12 m + 7 m coverage is outlined in white. The clusters NGC 602 B and NGC 602 B2 are marked with white dashed rectangles, and the massive O3 star Sk 183 is labeled.

across SGS 1, concluding that star formation in this section of the Wing has resulted from a combination of stochastic star formation mixed with some star formation stimulated by the expansion of SGS 1.

There is a supernova remnant (SNR) SXP 1062 projected ∼120 pc to the west of N90 centered around a Be/X-ray pulsar binary, with age estimates ranging between $(2–4) \times 10^4$ yr (Hénault-Brunet et al. 2012) and $(1–2.5) \times 10^4$ yr (Haberl et al. 2012); however, this remnant (see Figure 1(a); diameter ∼25 pc) has not yet reached N90 and is unlikely to be associated with star formation in the region. The cluster NGC 602 c (Westerlund 1964) and associated small, very faint H II region are located ∼190 pc to the northeast of N90 (Figure 1(a)), hosting the massive WO-type star Sk 188 and several other young, massive stars (Ramachandran et al. 2019). Given its distance, though, it too is unlikely to be directly related to recent star formation in N90.

The stellar population of N90 itself consists of a mixture of young stars concentrated around the central OB association NGC 602 and a scattered group of much older stars that are likely related to the general SMC field population. Figure 1(b) presents a closer view of NGC 602/N90, with two adjacent stellar concentrations to the north, NGC 602 B and NGC 602 B2, also identified; these clusters have estimated ages of up to 50–80 Myr and 47–160 Myr, respectively (Schmalzl et al. 2008; De Marchi et al. 2013). Through analysis of Hubble Space Telescope (HST) photometry, De Marchi et al. (2013) found that one-third of pre-main-sequence (PMS) stars in N90 itself are likely ≳30 Myr old and one-half are likely younger than 5 Myr.

The cause of the formation of the central cluster NGC 602 and more recent star formation event has been a subject of debate. Cignoni et al. (2009) found that the star formation rate (SFR) in N90 began to increase ∼10 Myr ago and has peaked

in the last ∼2.5 Myr. Using velocity maps derived from a survey of neutral hydrogen (Staveley-Smith et al. 1997) and optical and mid-IR (MIR) HST data, Nigra et al. (2008) suggested that compression and turbulence from the interactions of expanding H I shells ∼7 Myr ago is responsible for the formation of NGC 602 (with the northern shell corresponding to SGS 1). Alternatively, Fukui et al. (2020) proposed that compression resulting from a collision of two 500–600 pc radii H I clouds ∼8 Myr ago triggered the formation of NGC 602, and that SGS 1 is the disturbed region evacuated by this cloud collision.

Through analysis of HST optical and Spitzer Space Telescope (Spitzer) IR photometry, Carlson et al. (2007) and Carlson et al. (2011) concluded that NGC 602 formed ∼4 Myr ago, with a population of low-mass PMS stars forming ∼0.9 Myr later. They also identified 45 candidate young stellar objects (YSOs) and proposed that star formation has propagated outwards from NGC 602 to the "rim" of the H II region, with the youngest YSOs in N90 forming in the last ∼1 Myr. Gouliermis et al. (2007) and Gouliermis et al. (2012) analyzed the clustered spatial distribution of YSOs and PMS stars across N90 and suggested the formation of NGC 602 triggered progressive, ongoing star formation in the last 2.5 Myr in subclusters of PMS stars along the rim. Alternatively, De Marchi et al. (2013) suggested that a sequential star formation process, in which the formation of the earliest generations of young stars in the region did not significantly influence the formation of younger stellar generations, was more likely to have occurred.

New, high-resolution ($1''3$ or 0.4 pc) Atacama Large Millimeter/submillimeter Array (ALMA) data presented here clarify the amount and nature of dense gas in N90, and the history of the region's evolution. In Section 2, we describe the observations and analysis methods used. In Section 3, we

analyze the structure of small molecular clumps $\sim$2–23 pc from the central cluster, as well as their association with the populations of PMS stars and YSOs. We discuss if the clumps can reveal the formation history of the region, exploring signatures of large-scale H I collisions in SGS 1 as well as evidence for feedback from NGC 602 triggering ongoing star formation along the N90 rim. In Section 4, we examine common metrics of molecular cloud stability and star formation efficiency on the scales of both individual clumps and the entire region. We conclude in Section 5 with a discussion of the implications of our results for the evolution of N90, and compare star formation progression in N90 to solar-metallicity, higher-density environments.

2. Observations and Analysis

2.1. ALMA Data

The NGC602/N90 region was observed by ALMA project 2016.1.00360.S. A 150 point mosaic was observed with a 48 antenna compact configuration of the 12 m array (MOUS uid://A001/X88f/X2a2), for 49 minutes on source on 2016 December 30, with a mean precipitable water vapor (PWV) of 1.3mm. J0635-7516 (599 mJy at 230 GHz), J0334-4008 (432 mJy), and J0102-7546 (184 mJy) were used as a bandpass, amplitude, and phase calibrator, respectively. A slightly larger region of the sky was observed in a 60 point mosaic using the 7 m Atacama Compact Array (ACA) eight times between 2016 October 12 and 24, for a total of 416 minutes on source, mostly at a PWV of $\sim$0.5 mm. J0006-0623 (3.6 Jy at 230 GHz) or J0522-3627 (2.8 Jy) was used as a bandpass calibrator, Uranus as an amplitude calibrator, and J0450-8101 (1.6 Jy) as a phase calibrator. The spectral setup contains three spectral windows with 122.07 kHz channels each, centered on the ^{12}CO, ^{13}CO, and ^{12}C^{18}O $J = 2$–1 transitions. These windows have 1920 and 2048 channels and 234.4 and 250 MHz for the 12 and 7 m arrays, respectively. Additionally a 2 GHz wide, 128 channel spectral window centered at 232.86 GHz was observed. The native spectral channel spacing is 0.17 km s^{-1}, with a resolution of ^{12}CO of 0.184 km s^{-1}.

The data were processed with the ALMA Pipeline-CASA56-P1-B v42866 released with CASA 5.6.1-8 (McMullin et al. 2007), using the default recipes. Standard flagging resulted in 27% of the 12 m data and 35% of the 7 m data being flagged. The imaging stages of the ALMA pipeline correctly detected strong line emission and subtracted from the visibilities a linear fit to the continuum, excluding the line spectral ranges.

Calibrated visibilities from both arrays were imaged together using CASA::tclean, and Total Power data were also observed with ALMA and processed with Pipeline-Cycle4-R2-B packaged with CASA 4.7.0. The Total Power data were feathered with the interferometer data, but the interferometers alone recovered $>95\% \pm 5\%$ of the ^{12}CO 2–1 flux and $100\% \pm 10\%$ of the ^{13}CO 2–1 flux in the Total Power image (i.e., within the absolute calibration uncertainty), and the feathered image has a higher noise on large angular scales. Thus, we use the interferometer-only images for the clump analysis presented here. The combined 12 m + 7 m integrated intensity images in ^{12}CO 2–1 and ^{13}CO 2–1 are shown in Figure 2.

2.1.1. Clump Extraction

Molecular cloud emission is often decomposed into discrete "clumps" ($R \sim 1$ pc) or "cores" ($R \lesssim 0.1$ pc) to enable analysis of the characteristics of the complex structures within the clouds. Nonhierarchical clump identification methods like `clumpfind` (Williams et al. 1994) or `quickclump` (Sidorin 2017) segment position–position–velocity (PPV) cubes by identifying local maxima and assigning adjacent pixels above a minimum intensity $I_{\min}$ with a minimum intensity difference δI between the local maximum and the highest adjacent saddle point to discrete clumps. Diffuse molecular gas is typically not visible in observable CO emission in the SMC, as the low-metallicity, low dust-to-gas ratio, and higher interstellar radiation fields of the SMC result in observed CO emission being segmented into more discrete, "clumpier" structures (e.g., Muraoka et al. 2017; Jameson et al. 2018) than in the Milky Way or Large Magellanic Cloud (LMC) where filamentary structures are more common (e.g., Saigo et al. 2017; Indebetouw et al. 2020). Nonhierarchical methods like `clumpfind` are then more suited to environments like the SMC due to this tendency toward discrete CO structures.

We used a version of the `quickclump` python implementation[11] modified to include a parameter defining a required minimum peak intensity of a clump, $I_{\min pk}$ (Indebetouw et al. 2020).[12] The addition of this parameter ensures that clumps with relatively high signal-to-noise ratio (S/N) peaks are able to have emission in their envelopes assigned down to the level of the noise, which allows for the emission of the clump to be captured more completely, while avoiding introducing many additional clumps with low S/N peaks.

We applied the modified `quickclump` algorithm to the ^{12}CO observations, with a minimum intensity $I_{\min} = 4\sigma$, minimum change in intensity between leaves $\delta I = 3\sigma$, minimum peak intensity $I_{\min,pk} = 8\sigma$, and minimum number of pixels $n_{\min,pix} \simeq 2$ beams. Finally, we required that each clump have ^{12}CO velocity dispersions (as calculated in Section 2.1.4) greater than the spectral resolution for that line ($\sigma_v \gtrsim 0.18$ km s^{-1}). This yielded a total of 110 clumps.

2.1.2. Molecular Column Density

We assumed local thermal equilibrium (LTE) conditions to calculate column densities for clumps with significant ^{13}CO emission. Since many of the clumps identified in ^{12}CO do not appear to have strong corresponding emission in ^{13}CO, we required that clumps have a ^{13}CO S/N within the clump's ^{12}CO boundaries of S/N $\geqslant 3$ above 4σ to apply the LTE method. Our noise estimate was derived from the rms noise in the southern half of the cube ($\delta \lesssim 73°35'$) where no strong CO emission was detected in either line.

Only 29 of the 110 clumps (26%) fulfill this requirement, while the remaining 81 clumps (74%) do not possess any strong ^{13}CO emission. To overcome this obstacle, our mass estimation method takes place in two parts (described in this section and Section 2.1.3). Additionally, our mass estimation method is similar to the approach taken by Wong et al. (2022), who, in their study of the LMC's 30 Doradus region, found that 53% of CO-detected clumps were only traced by ^{12}CO and did not have corresponding ^{13}CO emission. The majority of the clumps in N90 with corresponding ^{13}CO emission are located in the northeast rim and nonrim sections near NGC 602, with
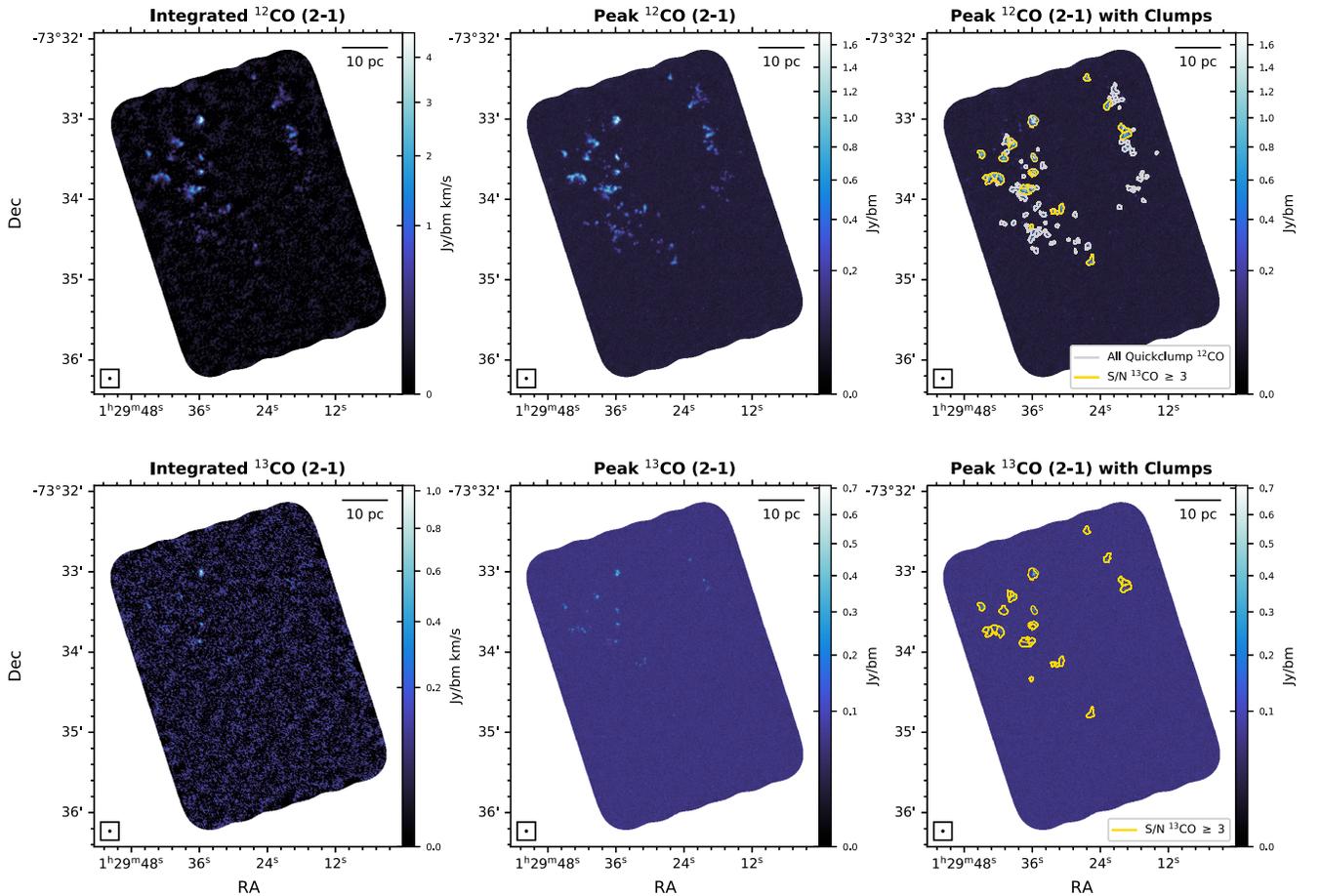
---

[11] https://github.com/vojtech-sidorin/quickclump/
[12] https://github.com/indebetouw/quickclump

Figure 2. Images of combined 12 m + 7 m ALMA ^{12}CO (2–1) and ^{13}CO (2–1) data. Top left: integrated ^{12}CO (2–1) intensity. Top center: peak ^{12}CO (2–1) intensity. Top right: peak ^{12}CO (2–1) intensity with contours of clumps identified by the `quickclump` algorithm in gray. Contours of the subset of these clumps with ^{13}CO (2–1) S/N $\geqslant$ 3 are in gold. Bottom left: integrated ^{13}CO (2–1) intensity. Bottom center: peak ^{13}CO (2–1) intensity. Bottom right: peak ^{13}CO (2–1) intensity with contours of ^{13}CO (2–1) S/N $\geqslant$ 3 clumps in gold. In all panels, the synthesized beam size is shown in the lower-left corner.

several others on the northwest rim near the massive O3 star Sk 183 (see definitions of these subregions in Figure 7(a)).

We assumed that ^{12}CO is optically thick and that its excitation temperature T_{ex} is a function of brightness temperature,

$$T_{ex} = \frac{11.1 \, \text{K}}{\ln\left(\frac{11.1}{I_{12} + 0.19} + 1\right)}, \qquad (1)$$

where I_{12} is the ^{12}CO(2–1) intensity in Kelvin. Since this result only relies on ^{12}CO emission, we derived this quantity for all clumps. Calculated T_{ex} range from 6.5–28 K (Figure 7(c)).

We assumed that ^{13}CO is optically thin, that ^{13}CO and ^{12}CO share the same T_{ex}, and that their relative abundance is constant. We found the ^{13}CO(2–1) optical depth of each PPV pixel for the 29 ^{13}CO-traced clumps as (Garden et al. 1991; Bourke et al. 1997; Indebetouw et al. 2013; Wong et al. 2017),

$$\tau_0^{13} = -\ln\left[1 - \frac{T_B^{13}}{10.6}\left\{\frac{1}{e^{10.6/T_{ex}} - 1} - \frac{1}{e^{10.6/2.7} - 1}\right\}^{-1}\right], \qquad (2)$$

and column density $N(^{13}$CO) as

$$N(^{13}\text{CO}) = 1.2 \times 10^{14} \frac{(T_{ex} + 0.88 \, K) \, e^{5.29/T_{ex}}}{1 - e^{-10.6/T_{ex}}} \int \tau_\nu^{13} d\nu. \quad (3)$$

The maximum $N(^{13}$CO) was 2.6×10^{16} cm^{-2}. We assumed an abundance ratio of H$_2$ to ^{13}CO of 1.25×10^6 following Jameson et al. (2018) for the SMC, such that $N(\text{H}_2) = 1.25 \times 10^6 \, N(^{13}\text{CO})$. This abundance ratio is the combination of ^{12}C/H and ^{12}CO/^{13}CO abundance ratios; the former is constrained by UV absorption measurements (see references in Tchernyshyov et al. 2015) to ±40%, and the latter by non-LTE modeling of CO emission lines at ~10 pc resolution (Nikolić et al. 2007), with another 40% uncertainty. The total ^{13}CO/H$_2$ could then be off by a factor of two, most likely in the direction that underestimates H$_2$. The maximum H$_2$ column density observed was 3.2×10^{22} cm^{-2}.

We calculated LTE masses for the clumps with significant ^{13}CO detections as

$$M_{\text{LTE}} = 1.36 \, m_{\text{H}_2} \sum N(\text{H}_2) \delta x \delta y, \qquad (4)$$

where 1.36 is a factor derived from cosmic abundances to convert from H$_2$ mass to total mass including helium, δx and δy are pixel sizes, and m_{H_2} is the mass of an H$_2$ molecule. LTE clump masses ranged from 13 $M_\odot$ to 286 $M_\odot$, with a median mass of 64 $M_\odot$ and total mass of all ^{13}CO-traced clumps of $2435 \pm 330 \, M_\odot$.

Of course, it is possible that the clumps are not in LTE. The systematic effects of using the LTE approximation can be understood by analyzing many non-LTE models. From large

grids of Radex (van der Tak et al. 2007) models, we find that under typical molecular cloud conditions, where ^{12}CO has optical depths of a few and ^{13}CO between $\sim$0.5 and 2, the LTE method tends to slightly (10%–20%) overestimate the ^{12}CO excitation temperature (since its optical depth is less than the infinite depth assumed). On the other hand, if ^{13}CO has an optical depth <1, its excitation temperature can be lower than that of ^{12}CO by up to a factor of two. For very cold clouds ($T_K \lesssim 10$ K), the LTE method underestimates the true ^{13}CO column density by up to a factor of $\sim$2, and for very dense ($n_H \gtrsim 5000$ cm^{-3}) and warm ($T_K \gtrsim 50$ K) clouds, the LTE method overestimates the ^{13}CO column density by up to a factor of $\sim$2. However, the calculated ^{13}CO column density from the LTE method is within 25% of the true value for fairly wide ranges of parameter space: ^{12}CO column densities between 10^{16} and 3×10^{18}, and 15 K $\lesssim T_K \lesssim 65$ K. For the N90 clumps that we apply the LTE method to, the average $N(^{12}$CO) is 5.9×10^{17}, and the average T_{ex} is 19 K, so we expect the LTE mass estimates to be reasonable.

2.1.3. CO-to-H$_2$ Conversion Factor

Although the LTE method described above is powerful when multiple lines are traced, it is limited and becomes less reliable for clumps with weak ^{13}CO detections. To circumvent this issue, we derived an X_{CO} CO-to-H$_2$ conversion factor from the clumps traced by ^{13}CO, and applied it to the 81 clumps with ^{13}CO S/N $\geqslant 3$ to obtain estimates of their masses. We use the notation $X_{CO,B}$ to indicate that this factor is only intended to include gas that is ^{12}CO-"bright," and does not account for diffuse "CO-dark" gas in clump envelopes. We discuss the role of CO-dark gas in N90 in Section 4.2.

We fit $X_{CO,B}$ as

$$N(H_2) = X_{CO,B} \, W_{12CO} \qquad (5)$$

where $N(H_2)$ is the total H$_2$ column density in units of cm^{-2}, and W_{12CO} is the integrated ^{12}CO line intensity in units of kelvin kilometers per second. In the Milky Way, Bolatto et al. (2013) recommended an average value of $X_{CO,MW} = 2 \times 10^{20}$ cm^{-2} (K km s^{-1})$^{-1}$. We performed ordinary least-squares regression with a heteroskedasticity-consistent standard error estimator ("HC3" in the python package statsmodels; Seabold & Perktold 2010). The best-fit slope was $X_{CO,B} = (3.4 \pm 0.2) \times 10^{20}$ cm^{-2} (K km s^{-1})$^{-1}$, or equivalently $X_{CO,B} \sim 1.7 \, X_{CO,MW}$.

This fit is shown in Figure 3. The 95% confidence interval for $X_{CO,B}$ is $[3.0 \times 10^{20}, 3.75 \times 10^{20}]$ cm^{-2} (K km s^{-1})$^{-1}$, and standard fit diagnostics suggest this model is adequate (coefficient of determination $R^2 = 0.95$, F-test statistic calculated for robust covariance of $F = 309.8$ with $p < 0.001$). The $X_{CO,B} \sim 1.7 \, X_{CO,MW}$ we derived is consistent with, albeit slightly lower than, values of $X_{CO,B}$ found in other SMC regions observed at parsec-scales in ^{12}CO and/or ^{13}CO. In the Magellanic Bridge, Kalari et al. (2020) and Valdivia-Mena et al. (2020) derived values of X_{CO} of $\sim$2–4 $X_{CO,MW}$, while Muraoka et al. (2017) found $X_{CO} \sim 4 \, X_{CO,MW}$ in the star-forming region N83C in the southeast Wing. Jameson et al. (2018) similarly found an average $X_{CO} \sim 5 \, X_{CO,MW}$ across several star-forming regions in the southwest Bar of the SMC at <3 pc scales.

We applied our derived $X_{CO,B}$ factor to the clumps without significant ^{13}CO detections and derived masses $M_{X_{CO,B}}$ ranging

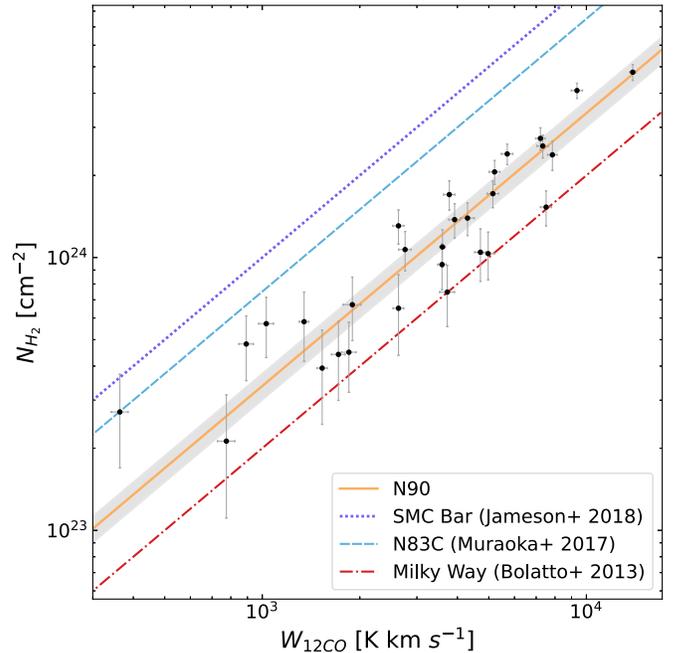**Figure 3.** Total column density $N(H_2)$ is compared to total integrated ^{12}CO intensity W_{12CO} for clumps with ^{13}CO S/N $\geqslant 3$. The solid orange line shows the best-fit CO-to-H$_2$ conversion factor $X_{CO,B}$ for the clumps in N90, $X_{CO,B} = (3.4 \pm 0.2) \times 10^{20}$ cm^{-2} (K km s^{-1})$^{-1}$, and is surrounded by gray shading that shows the 95% confidence interval for the fit. The dotted purple line was fit to star-forming regions in the SMC Bar by Jameson et al. (2018), with $X_{CO} = 1 \times 10^{21}$ cm^{-2} (K km s^{-1})$^{-1}$. The dashed blue line was fit to clumps in N83C in the SMC Wing by Muraoka et al. (2017), with $X_{CO} = 7.5 \times 10^{20}$ cm^{-2} (K km s^{-1})$^{-1}$. The dotted–dashed red line shows a typical $X_{CO} = 2 \times 10^{20}$ cm^{-2} (K km s^{-1})$^{-1}$ for the Milky Way (Bolatto et al. 2013).

between 1.2 and 52 $M_\odot$, with a mean value of 10.7 $M_\odot$ and total mass of 860 $M_\odot$. We also applied this factor to the clumps traced by ^{13}CO. Going forward, we use the $M_{X_{CO,B}}$ mass estimates for all clumps for consistency. We find a total gas mass for all clumps traced by ^{12}CO in N90 of $M_{X_{CO,B}} \sim 3310 \pm 250 \, M_\odot$. The 26% of clumps that are traced by ^{13}CO contribute 74% of the total CO-bright clump mass.

Our mass estimate is slightly lower than the total clump mass estimate of 3800 $M_\odot$ in N90 made by Fukui et al. (2020) using only the 7 m ^{12}CO ALMA observations. The difference between these results stems from variations in mass calculation and clump identification methods, not in spatial filtering, because >95% of the ^{12}CO flux in the 7 m map is recovered in our 12 + 7 m map. Fukui et al. (2020) identified 19 clumps with radii between 1.9 and 3 pc and used an $X_{CO,B} = 7.5 \times 10^{20}$ cm^{-2} (K km s^{-1})$^{-1}$ (Muraoka et al. 2017), as opposed to our sample of 110 clumps with radii between 0.2–0.8 pc and lower adopted $X_{CO,B}$.

2.1.4. Other Clump Properties

A full catalog of clump properties is presented in machine-readable format in Table A1. We determined the radius R of each clump by fitting an ellipse to its half-light contour and converting the FWHM values of the ellipse's major and minor axes to the standard deviation of a Gaussian profile. We then multiplied by 1.91 to calculate the "effective radius" as defined by Solomon et al. (1987). We report radii as the geometric mean of the major and minor axes, and these values range from 0.26–0.77 pc with a median of 0.40 pc.

We calculate average surface densities as $\Sigma = M_{X_{CO,B}}/(\pi R^2)$. The median Σ is 24 $M_\odot$ pc^{-2}, with a standard deviation of 40 $M_\odot$ pc^{-2}. To estimate the volume densities of clumps, we assume that the clumps follow a power-law density profile,

$$\rho(r) = \rho_c \left(\frac{r}{R_0}\right)^{-k}, \qquad (6)$$

where R_0 is a normalizing radius that we set to be $R_0 = 0.1$ pc for all clumps, and ρ_c is the density of the clump at R_0. Using the derivation in Appendix A.1 of O'Neill et al. (2022), this central density can be estimated as

$$\rho_c = \frac{(3-k)}{4\pi} \frac{M(r)}{R_0^k \, r^{3-k}}. \qquad (7)$$

Power-law indices of $k \sim 1$–2 have frequently been derived for clumps and cores (e.g., Caselli et al. 2002; Pirogov 2009; Chen et al. 2019, 2020; Lin et al. 2022), and we adopt $k = 1$ for the N90 clumps. Through solving Equation (7) with $r = R_{CO}$, densities at 0.1 pc range between 10^1–10^3 $M_\odot$ pc^{-3}, with an average of $\rho_c \simeq 190 \, M_\odot$ pc^{-3}.

We calculated velocity dispersions σ_v and peak CO velocities v_{LSRK} by fitting Gaussian distributions to intensity-weighted ^{12}CO velocity profiles. We do not correct σ_v for the expected contribution from thermal motion (~ 0.08 km s^{-1} for CO at 20 K); this is discussed further in Section 4.1. Values of σ_v ranged from 0.23–1.07 km s^{-1} with a median of 0.45 km s^{-1}. Peak ^{12}CO velocities ranged between $v_{LSRK} = 159$ and 179 km s^{-1}, with a mean of 167 km s^{-1}.

2.2. Archival Data: IR-identified YSO Candidates

Two types of YSOs have been analyzed in the N90 region: solar-mass PMS stars identified with high-resolution HST optical and near-IR photometry, and YSO candidates with infrared excess emission attributed to circumstellar dust identified using Spitzer and Herschel Space Telescope (Herschel) data. We revisit these populations here in order to assess their relationship with the resolved molecular gas, but do not attempt to redo the careful classification of previous authors.

2.2.1. HST Data

We used HST F555W ($\sim V$) and F814W ($\sim I$) observations of N90 reduced by Schmalzl et al. (2008) to study the distribution of solar-mass PMS stars in the region, as selected by Gouliermis et al. (2012, hereafter G12). The locations of PMS stars are shown in Figure 4. The data from HST GO program 10248 consist of 2156 s and 2269 s total integration time with the Advanced Camera for Surveys (ACS) Wide Field Camera (WFC) in F555W and F814W, respectively. Photometry was performed using DOLPHOT,[13] reaching a depth of 26 mag in each filter, albeit at reduced completeness below 23 and 22.5 mag in F555W and F814W, respectively (see Schmalzl et al. 2008, for details).

G12 separated faint PMS stars from lower main-sequence stars by fitting pairs of Gaussians to the distribution of stars contained within bands perpendicular to the main sequence. The

---

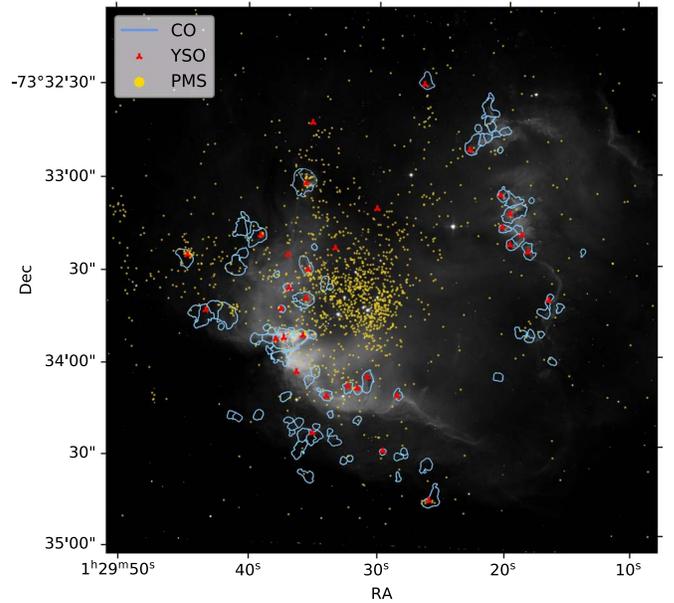[13] The ACS module of DOLPHOT is an adaptation of the photometry package HSTphot (Dolphin 2000). It can be downloaded from http://americano.dolphinsim.com/dolphot/.

Figure 4. The HST ACS Hα image is shown with the locations of PMS stars (yellow points), YSO candidates (red triangles), and the 2D boundaries of the CO clumps identified by the quickclump algorithm (light blue contours).

minimum between the Gaussian corresponding to the main-sequence population and that corresponding to the redder PMS population is taken as the classification boundary. We select PMS stars as falling within or to the right of the region bounded by F814W > 21.8 mag and F814W < -1.9(F555W—F814W)^2 + 8.3(F555W—F814W) + 16.6. We generated isochrones using the Pisa PMS evolutionary models (Tognelli et al. 2011) and the IDL program TA-DA (Da Rio & Robberto 2012) to create synthetic photometry based on the Kurucz (1993) atmospheric models. The models were calculated for $Z = 0.003$, $Y = 0.254$, and mixing length parameter $\alpha = 1.2$. We assumed $A_V = 0.25$ mag and $E(B-V) = 0.08$ mag (Carlson et al. 2007; Gouliermis et al. 2012), $R_V = 3.1$ (Schultz & Wiemer 1975; Gordon et al. 2003), and a distance modulus of $\mu = 18.91$ mag (corresponding to ~ 60.6 kpc; Hilditch et al. 2005). We assigned ages to each PMS star based on the track it was closest to for ages between 0.5 and 6.5 Myr in 0.25 Myr steps.

The resulting isochrones for ages of 0.5, 1, 1.5, 2.5, 3.5, 5, and 6 Myr are shown in Figure 5 with the selected PMS stars. In Section 3.3.2, we estimate an average $A_V \simeq 3.1$ mag through the centers of CO clumps that contain PMS stars. For the $\sim 10\%$ of PMS stars that appear contained within a projected 2D clump, a typical embedded star in the center of a clump might then reasonably be affected by half of this value, $A_V \simeq 1.6$ mag. Reddening vectors for both $A_V = 0.25$ mag and $A_V = 1.6$ mag are plotted in Figure 5. They fall at steep angles to the isochrones and indicate that high levels of differential reddening could significantly skew age estimates. We discuss this possibility further in Section 3.3.2.

2.2.2. Spitzer and Herschel Data

We also reanalyzed Spitzer-identified intermediate- and high-mass YSO candidates in the region. Carlson et al. (2011, hereafter C11) combined V, I, J, H, K, Spitzer IRAC 3.6–8.0 μm, and Spitzer MIPS 24 μm photometry, using the high-resolution optical data to remove background galaxies. C11 first fit the sources with stellar photospheres, removing
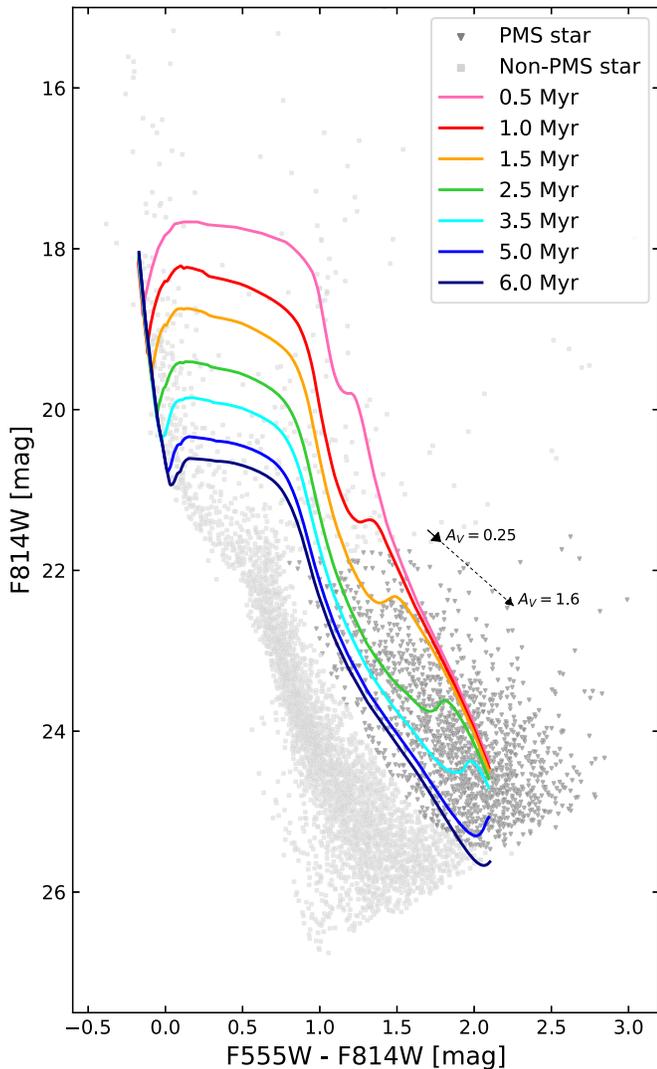
Figure 5. Locations of stars in F555W—F814W, F814W color–magnitude space. PMS stars are marked with dark gray triangles, and non-PMS stars are marked with light gray squares. PMS isochrone models for ages between 0.5 and 6 Myr are shown as colored curves. A reddening vector for $A_V = 0.25$ mag is shown by the thick black solid arrow, and for $A_V = 1.6$ mag by the thin black dashed arrow.

an annulus around each aperture was subtracted. The aperture photometry agrees within uncertainties with the previous C11 photometry for most sources, except those that suffer from confusion and crowding.

We visually assessed the spectral energy distribution (SED) and image cutouts in all filters using a script to assemble that information on a single page for each source, in order to evaluate which filters were contaminated by neighboring sources and/or diffuse emission; in the case of contamination, we used the aperture flux density as an upper limit in subsequent fitting. After this assessment, most of the sources had to be fit with upper limits in the new longer-wavelength bands because of the lower angular resolution of those data; however, these upper limits are still sufficient to exclude some models included in C11 that are very bright in the far-infrared (FIR).

We fit the sources with the updated Robitaille (2017) set of YSO models, which cover a wider range of parameter space more uniformly than the previous Robitaille et al. (2006) grid. However, the newer models do not have associated stellar masses as the 2006 models did, so we match each model's log L and log T to the nearest PARSEC PMS photosphere model (Bressan et al. 2012) to determine an $M_\star$. The new set of models are parameterized by envelope characteristic density ρ_0 and centrifugal radius R_C. Given that the circumstellar envelope has the particular density distribution of a rotating infalling toroid, one can uniquely calculate an "envelope accretion rate" $\dot{M}$ for a model's given ρ_0, R_C, and stellar mass. This parameter is largely a convenient way to parameterize the degree to which the source is embedded, with higher $\dot{M}/M_\star$ indicating a more embedded source as discussed in Robitaille et al. (2006). When we compare these properties to CO clumps in Section 3.3.1, the general properties of the YSO candidate population will be considered, but the precise fitted mass or envelope mass will not dramatically alter our conclusions.

For each source, we calculate χ^2 for each model, and use the probability-weighted mean value of each fit parameter and the FWHM of the parameter's 1D marginalized probability density function (PDF) as the fitted parameter and its uncertainty. We examined all sources' PDFs as a function of $M_\star$ and envelope $\dot{M}$: a minority of sources have multiply peaked PDFs, but the adopted uncertainty range in all cases encompasses both peaks so is a reasonable measure of the data's ability to constrain the source properties.

Our reanalysis does not change the list of intermediate-mass YSO candidates relative to C11. The primary addition to C11's analysis is that the addition of longer-wavelength upper limits eliminates luminous, heavily embedded models, with high circumstellar dust columns. Addition of longer-wavelength photometry in a few cases suggests an infrared excess for some sources classified by C11 as bare stellar photospheres, but none of these additions are definitive, and higher-resolution long-wavelength imaging will be required to conclusively measure any infrared excess.

We preserve C11's classification of "K" source as non-YSOs in our analysis: K049 (J012903.28-733413.2) has a tentative 100 μm detection of 35 ± 15 mJy, but is located in filamentary diffuse emission. K194 (J012920.73-733327.1) has a marginal 100 μm measurement of 4.5 ± 3 mJy. The most likely IR-excess candidate among C11's "K" sources is K456 (J012954.82-733231.5) with a marginal 100 μm measurement of 2.7 ± 1.6 mJy, but also a 24 μm flux of 1.1 ± 0.45 mJy in

sources consistent with stars, and then fit the remainder with Robitaille et al. (2006) YSO models to identify and classify all sources consistent with intermediate-mass YSOs. Starting with the C11 combined photometry catalog with galaxies removed, but including sources they classified as stars, we added aperture photometry from the Herschel HERITAGE survey (Meixner et al. 2013; Seale et al. 2014) at 100, 160, 250, and 350 μm using the Spectral and Photometric Imaging Receiver (SPIRE) and Photodetector Array Camera and Spectrometer (PACS).

We recalculated aperture photometry of all Spitzer and Two Micron All Sky Survey images in order to directly compare our aperture photometry code against the catalog photometry, and have a consistently calculated number for all bands in which an upper limit was required. Our script simply extracts the pixel sum in circular apertures at the source location, with radii of [1, 1, 3, 3, 3, 3, 9, 18, 8, 11, 18, 25, 37] arcseconds in filters [F555W, F814W, IRAC1, IRAC2, IRAC3, IRAC4, MIPS24, MIPS70, PACS100, PACS160, SPIRE250, SPIRE350, SPIRE500]. A background consisting of the median value in

excess of a stellar photosphere. All three lie outside of the region mapped in CO, so their classification has no effect on our conclusions. C11 noted two sources that they called stars but with infrared excess emission in their analysis with a longest wavelength of 24 μm. S235 and S213 are relatively bright stars located within the central bubble; we confirm that both have 24 μm emission in excess of a photosphere, but neither are conclusively detected at longer wavelengths, as they would be if they had a massive circumstellar envelope. Thus, we keep the C11 "star" classification. Neither is associated with CO emission.

The longer-wavelength data do, however, significantly change the stellar and envelope masses for the most massive sources—all of the most massive sources fit by C11 are fit with models that have bright FIR excess emission. And in all cases, we measured the FIR emission to be modest, excluding those massive models that are acceptable fits to C11's shorter wavelength range. The largest fit YSO mass is 8 ± 1 $M_\odot$, whereas C11's best fits included one object consistent with 26 $M_\odot$ (we find 4 ± 1 $M_\odot$) and five with masses between 10 and 12 $M_\odot$. In total, we find a higher mass estimate than C11 for only one YSO (Y227, J012937.37-733352.4, with C11's mass of 6.86 $M_\odot$ versus our estimate of 6.99 $M_\odot$); all other YSO candidates have lower masses. We derived a total YSO mass of $\sim 160\, M_\odot$ in N90, which is significantly less than C11's previous estimate of a total YSO mass of $\sim 300\, M_\odot$. The fit properties of all YSOs are reported in Table A2.

Our fits to the Robitaille models yield two constraints on the age of the intermediate-mass YSO candidates: the age of the PARSEC photospheric model matched with each Robitaille (2017) YSO model, and the fitted mass divided by fitted envelope accretion rate. The photospheric age is fairly well constrained, to $\sim 10^5$ yr for the more massive YSOs >5 $M_\odot$, increasing to $\sim 10^6$ yr for the lower-mass $M_\star \simeq 2 M_\odot$ YSOs. The fitted mass divided by accretion rate is consistent, agreeing to within the order-of-magnitude uncertainties on that ratio, but has the even larger caveat that the current fitted accretion rate is almost certainly not the accretion rate through the entire mass assembly of the YSO, and that the fitted accretion rate only has physical meaning insofar as the rotating infalling envelope density distribution used by Robitaille actually represents the accretion process. In general, we are far more confident that this fitting process can constrain the total envelope dust mass than we are in interpreting that quantity as an accretion rate. Nevertheless, these two constraints suggest ongoing intermediate-mass star formation in NGC 602 over the last 1–2 Myr.

3. Dynamics and Evolution of N90

3.1. Morphology of N90

N90 is characterized by a ring-shaped "rim" ~ 30 pc in diameter that frames a central cavity containing NGC 602 (Figure 1(b)). The rim is most clearly visible to the east and west, with the northeast section of the rim appearing to be more diffuse and the southeast section denser. Many background galaxies are clearly visible outside the edges of N90 due to the low surface density, generally transparent surrounding environment of the SMC Wing ($A_V \lesssim 1^{-2}$ on degree scales; Gordon et al. 2014).

N90's rim displays clear evidence of photodissociation and has many "pillar"-like features. Most of the molecular clumps
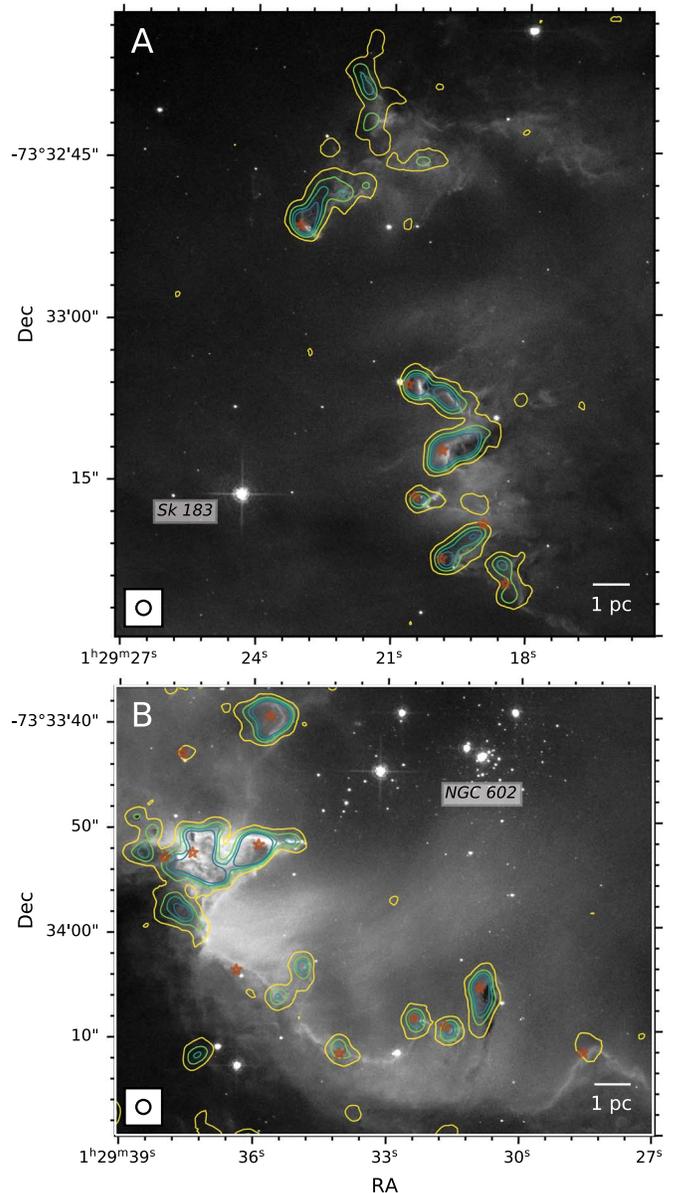
Figure 6. Top: expanded image of Figure 7(a)'s Region A, along the west rim near the massive star Sk 183 (labeled). Contours of integrated ^{12}CO intensity are shown, with levels of 0.25, 0.5, 0.75, and 1 Jy beam^{-1} km s^{-1} drawn in yellow, green, teal, and blue, respectively. The synthesized beam size for the CO observations is shown in the lower-left corner. The locations of YSO candidates are shown by red stars. The HST ACS Hα image is shown in gray. Bottom: the same as in the left panel, but for Figure 7(a)'s Region B, on the east rim near NGC 602 (labeled).

in N90 are arranged along or immediately outside of the rim, and many of the pillars are closely associated with CO emission. Two representative regions of the rim are shown in Figure 6. CO emission closely traces the edges of the Hα emission, and most of the pillars point toward the center of N90; this suggests that they are the result of radiation from the cluster NGC 602 (Gritschneder et al. 2010).

Many of the YSO candidates in N90 (Section 3.3.1) are embedded within the pillars and clumps along the rim. In their study of ~ 200 giant molecular clouds (GMCs) in the LMC, Ochsendorf et al. (2016) found that massive star formation is most likely to occur at the edges of clouds nearest to young stellar clusters, implying these clusters stimulate clump and star

Figure 7. Spatial variation of CO clump characteristics, with the HST Hα image shown in gray. (a) The regions we define as part of the rim are shown in gre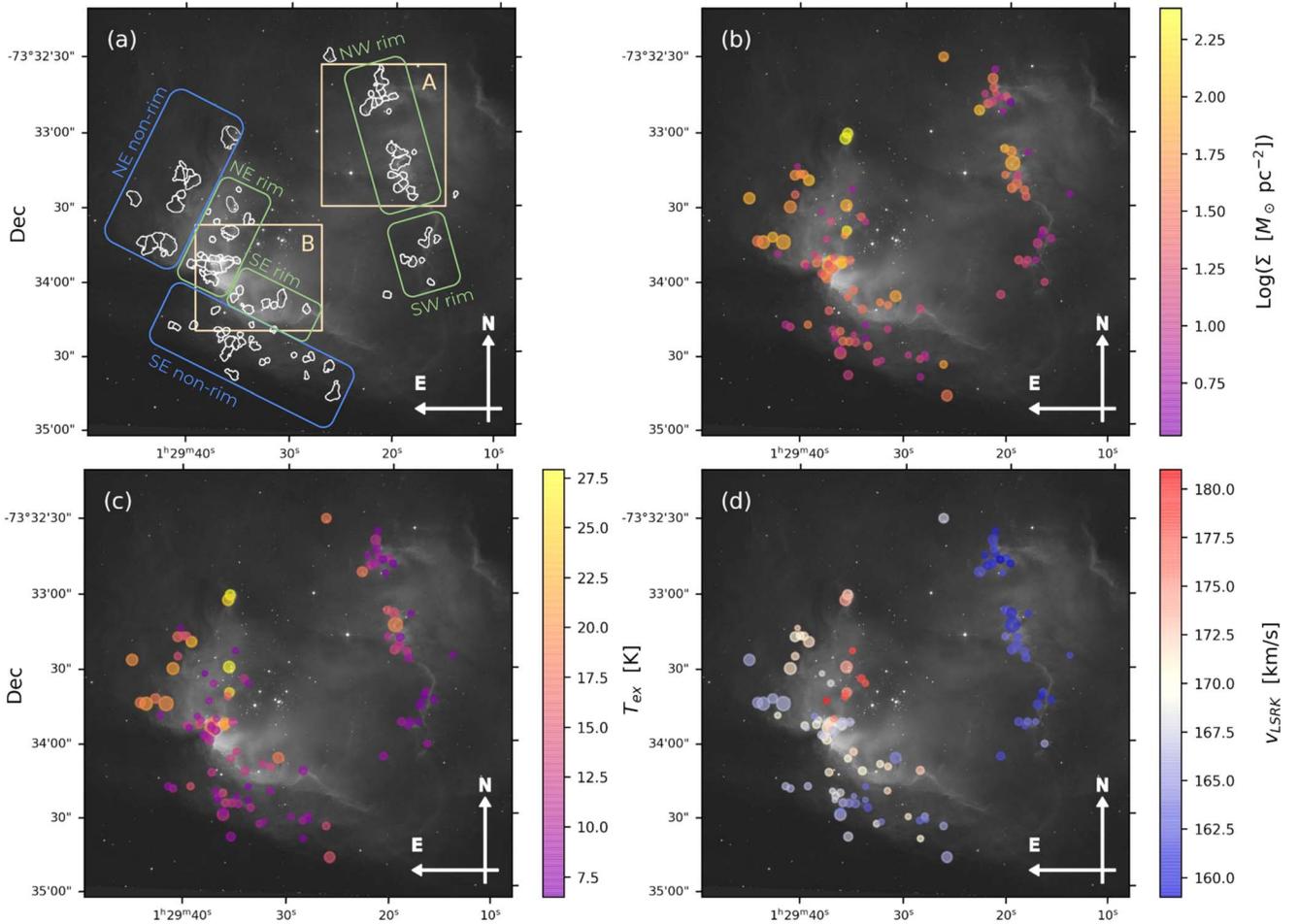en, and the corresponding nonrim regions are marked in blue. The 2D clump boundaries identified by the quickclump algorithm are shown in white. Details of the two orange rectangles A and B are shown in Figure 6. (b) Average surface density Σ of clumps, with point sizes proportional to clump area. (c) Maximum clump excitation temperature T_{ex}. (d) Peak ^{12}CO velocity of clumps, with the red/blue color scale centered at the mean radial velocity (RV) of H I components surrounding N90, $v_{LSRK} \sim 170$ km s^{-1}, as derived from Fukui et al. (2020) and Nigra et al. (2008).

formation. The YSO candidates in N90 shown in Figure 6 are also mostly concentrated on the edges of the rim/their host pillars that are closest to NGC 602 or Sk 183; this is especially apparent in Region A.

We assess whether the formation of the YSOs in N90 may have been triggered by NGC 602. Here we define triggered star formation as a process in which the interaction between the earliest generation of stars and their environment directly causes the formation of subsequent generations. This stands in contrast to sequential star formation scenarios where the formation of distinct stellar generations is largely unrelated.

3.2. Spatial Variation in Clump Properties

We assessed visually which CO clumps are on the rim (Figure 7(a)) to investigate if any trends between clump properties and 2D position relative to the rim exist. Through this assessment, we estimate that 64 of the clumps are on the rim, and 46 are outside of it. Seventy-six of the clumps are located in the eastern half of the region nearer to the NGC 602 cluster, and 34 are in the western half nearer to the massive star Sk 183. The spatial variation of the column densities, excitation temperatures, and radial velocities (RVs) of the CO clumps is shown in Figures 7(b)–(d).

Clumps in the northeast, both in the rim and nonrim sections, appear to have higher surface densities (Figure 7(b)) and excitation temperatures (Figure 7(c); which, under the LTE assumptions, are indirectly equivalent to ^{12}CO brightness temperature) than clumps along the southeast rim and nonrim sections. The northeast clumps may thus be more directly affected by the central OB association NGC 602, as gas associated with the Hα rim could present less of a barrier to mechanical and radiative heating from the association than for clumps shielded by (and possibly located within or behind) dense gas to the south. We used 2D radial distances between the center of NGC 602 ($\alpha = 01\ 29\ 32.133$, $\delta = -73\ 33\ 38.13$) and all clumps on the eastern half of N90 as a proxy for the true 3D distances between their positions. We calculated Spearman's rank correlation coefficient ρ_s between the distance from NGC 602 and clump properties; there are weak-to-moderate negative correlations between distance and σ_v ($\rho_s = -0.40$, $p < 0.001$) and distance and v_{LSRK} ($\rho_s = -0.58$, $p < 0.001$), and only weak correlations between distance and R, $M_{X_{CO,B}}$, or T_{ex} (all $|\rho_s| < 0.3$).

Along the western rim, the warmest and densest clumps are concentrated in the northwest section near the massive O3 star Sk 183 ($\alpha = 01\ 29\ 24.6$, $\delta = -73\ 33\ 16.43$). Although the

clumps in the northwest are relatively removed from NGC 602 itself, their proximity to Sk 183 could be responsible for their marginally higher excitation temperatures relative to the cooler and more isolated clumps in the southwest rim. Evans et al. (2012) found that Sk 183 is likely responsible for the majority of hydrogen-ionizing photons in N90, and Ramachandran et al. (2019) confirmed its outsized effect, with Sk 183 contributing up to 30% of all ionizing photon flux in their sample of $\sim$300 OB stars scattered throughout the entirety of SGS 1. We stacked the CO spectra within 5 pc of Sk 183 and identified no significant ($>3\sigma$) emission in either ^{12}CO or ^{13}CO. This suggests that it has successfully dissociated its immediate surroundings, and could even be responsible for the nearby northern "gap" in the Hα rim. We also explored correlations between western clump properties and their distance from Sk 183, and found moderate negative correlations between distance and σ_v ($\rho_s = -0.51$, $p = 0.002$); $M_{X_{CO,B}}$ ($\rho_s = -0.48$, $p = 0.004$); and T_{ex} ($\rho_s = -0.49$, $p = 0.003$).

Figure 8 compares the distributions of T_{ex}, σ_v, R, and Σ between all rim and nonrim clumps. The PDFs of these properties are represented using Gaussian kernel density estimations (KDEs), with bandwidths chosen using "Scott's Rule" as implemented in the Scipy python package (Virtanen et al. 2020). By performing Kolmogorov–Smirnov (K-S) tests comparing the properties of rim versus nonrim clumps, we found no significant differences between the distributions of R (with a p-value of $p = 0.43$ at a significance level requirement of $\alpha = 0.05$), T_{ex} ($p = 0.26$), or Σ ($p = 0.682$) for the two groups. There was a significant difference in the distributions of σ_v between rim and nonrim clumps ($p = 0.002$), with a one-sided Mann-Whitney U-test revealing that clumps along the rim on average have larger σ_v ($p = 0.003$).

The overall lack of any strong correlations and relatively few significant differences between groups suggests that stellar feedback (e.g., radiation pressure or stellar winds) has not had a significant differential impact on the physical properties of the molecular clumps, or at least that any systematic trend cannot be extracted from the random cloud property variations with the modest range of central cluster distances available in these data ($\sim$2–23 pc). Indebetouw et al. (2013) found a similar lack of significant trends from 10–25 pc from the cluster R136 in the LMC region 30 Doradus.

3.2.1. Clues for Formation of NGC 602

We stacked the CO spectra in the half of the ALMA coverage to the south of N90 ($\delta \lesssim -73°35'$), where no clumps were identified by the `quickclump` algorithm. We found no significant ($>3\sigma$) CO emission in this area. Assuming $T_{ex} = 10$ K, the mean $N(^{12}CO)$ in this region is less than 4.5×10^{16} cm^{-2}. Thus, we find no strong evidence for CO to the south of N90 and conclude that CO-traceable molecular gas is largely localized in the site of massive star formation to the north, which is adjacent to the southern rim of SGS 1. This correspondence suggests that turbulence and compression resulting from the southward expansion of H I component(s) within SGS 1 triggered both the formation of dense molecular gas and then stars in N90.

Fukui et al. (2020) proposed that the collision of two clouds hundreds of parsecs in diameter was responsible for the formation of NGC 602. In this scenario, the larger of their two H I clouds would have moved south from the northeast before colliding with a smaller, less-massive cloud moving north from
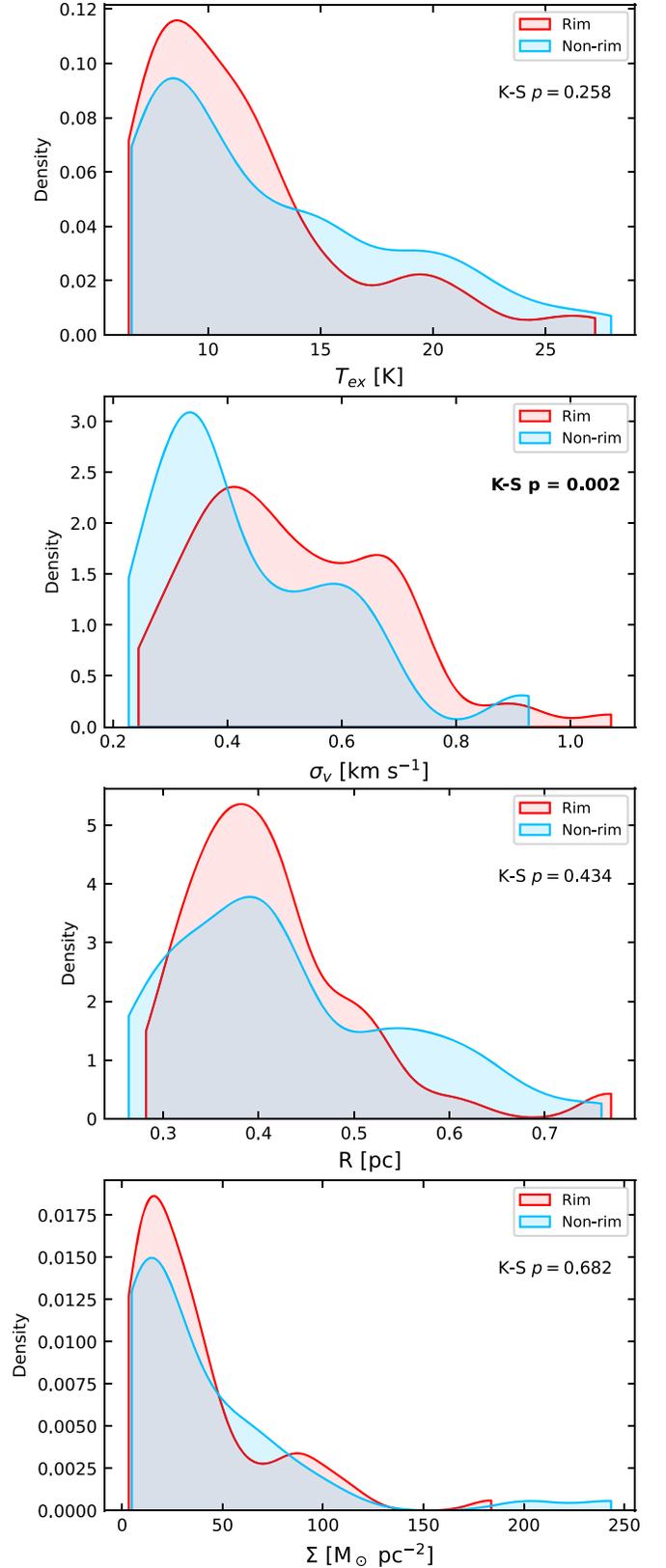
Figure 8. Kernel density estimations (KDEs) comparing physical properties of clumps on the N90 rim (red) and not on the N90 rim (blue), with both groups assigned as in Figure 7(a). p-values resulting from two-sided K-S tests comparing the rim vs. nonrim distributions are shown in each panel, with any $p < 0.05$ set in bold to indicate that there is a statistically significant difference between the distributions. Top: excitation temperature T_{ex}. Second from top: velocity dispersion σ_v. Third from the top: radius R. Bottom: surface density Σ.

the southwest. They suggested that SGS 1 is simply a cavity inside the more massive cloud created by this collision. In the alternative colliding shells formation scenario proposed by Nigra et al. (2008), one shell moved south from the northwest and the other moved south from the northeast, with NGC 602 forming at their intersection.

We examine if evidence of these collisions in SGS 1 7–8 Myr ago could still be preserved within the current clumps. At solar metallicity, photoelectric heating rates in molecular gas are usually sufficiently higher than energy injection rates from the decay of turbulence that a relationship between dissipation of turbulence and kinetic temperature is not expected. Mechanical heating can be traced by kinetic temperature when the heating is particularly high, as in central starbursts (e.g., Kazandjian et al. 2016; Mangum et al. 2019). At low metallicity, however, both cooling rates and photoelectric heating rates are sufficiently reduced that even more modest levels of turbulent dissipation might be able to affect the gas kinetic temperature.

Turbulence is expected to dissipate on the order of a crossing time (Elmegreen & Scalo 2004). The H I clouds considered in Fukui et al. (2020) have diameters $d \sim 600$ pc, velocity dispersions $\sigma_v \sim 10$ km s^{-1}, masses $M \sim 8 \times 10^6 M_\odot$, and, thus, a mean volume density $<n_{\rm H}>$ of 3 H cm^{-3}. The shell most closely associated with N90 by Nigra et al. (2008) has $d \sim 200$ pc, $\sigma_v \sim 6$ km s^{-1}, $M \sim 3 \times 10^5 M_\odot$, and also $<n_{\rm H}> = 3$ H cm^{-3}. Estimating a turbulent dissipation rate as $0.5 < \rho > \sigma_v^2 /\tau_{\rm crossing}$ with $\tau_{\rm crossing} \sim d/\sigma_v$ yields 1×10^{-27} and 3×10^{-27} erg s^{-1} cm^{-3} for the Nigra et al. (2008) and Fukui et al. (2021) clouds, respectively. The cooling rate for the neutral interstellar medium dominated by C$^+$ and O^0 line emission at $1/5$ $Z_\odot$ is $\lesssim 10^{-26}$ erg s^{-1} cm^{-3} in clouds at these low densities (Wolfire et al. 1995). These estimates are sufficiently uncertain as to preclude a definitive statement, but the cooling rate exceeding the estimated heating rate suggests that any excess kinetic energy from the cloud collision has probably been radiated away, and feedback from the central cluster and Sk 183 is still more likely the dominant energetic driver. However, it is not impossible that at low metallicity, the signature of more turbulent H I gas might still be present in current properties of the molecular gas formed from that H I gas.

We compare the RVs of the clumps to nearby stars in N90 and to SGS 1's proposed H I components. All velocities are reported in the LSRK frame. Clump RVs range from 161–179 km s^{-1}, with a mean of 168 km s^{-1}. Evans et al. (2012) derived an RV of 151 ± 1 km s^{-1} for Sk 183, and Ramachandran et al. (2019) derived a mean RV for $\sim$17 OB stars in N90 of 158 ± 4 km s^{-1}. The cause of this offset from the RVs of the CO clumps is unknown. The Ramachandran et al. (2019) measurements have typical uncertainties of ± 10 km s^{-1}, making it difficult to tell how significant this shift is. In contrast, the clump RVs are in close agreement with the RVs of nearby H I structures along the "ring" of SGS 1: Nigra et al. (2008) derived an RV of 168 ± 5 km s^{-1} for a proposed progenitor H I gas clump "curled" around the south of N90. Similarly, the larger of the two Fukui et al. (2020) clouds had a range of velocities from 163–183 km s^{-1}, with a peak at $\sim$173 km s^{-1}.

In Figure 7(d) we show the spatial variation of the clump RVs relative to the mean of these two measurements, 170 km s^{-1}. Clumps along the eastern rim near NGC 602

appear consistent with this value (median $+0.2$ km s^{-1} from 170 km s^{-1}), while clumps in the northeast and southeast nonrim regions (median -3.1 km s^{-1}) and the western half (median -7.7 km s^{-1}) mostly appear blueshifted. Gvaramadze et al. (2021) derived a central RV of 177 ± 6 km s^{-1} for background Hα emission near SNR SXP 1062, which falls just outside of the SGS 1 H I "ring." Since these measurements of H I and Hα RVs along SGS 1 are largely consistent with the RVs of the clumps in N90 on the edge of the ring, a close connection between SGS 1 and the formation of N90 appears likely.

3.3. Clump Association with YSOs and PMS Stars

Many previous studies have analyzed the characteristics of candidate PMS stars and YSOs in N90 (e.g., Carlson et al. 2007, 2011; Gouliermis et al. 2007, 2012; Schmalzl et al. 2008; Cignoni et al. 2009; De Marchi et al. 2013). To better inform our analysis of the observed CO clumps, we replicate and extend some aspects of this extensive past analysis. Hereafter, we refer to the candidate several-solar-mass sources with MIR excess emission selected from Spitzer and Herschel as "YSOs," and the generally lower-mass sources selected from their location in an HST color–magnitude diagram (CMD) as "PMS stars."

3.3.1. YSOs

Of the 33 YSOs identified in Section 2.2 that are inside the ALMA-observed area, 28 are located inside the projected 2D boundaries of a CO clump ($\sim$85%). Correspondingly, 27 of the 110 clumps ($\sim$25%) appear to contain at least one YSO. By performing one-sided K-S tests, we found significant differences between the properties of clumps that contain versus do not contain YSOs: clumps containing YSOs have higher R ($p < 0.001$), σ_v ($p < 0.001$), $M_{X_{\rm CO,B}}$ ($p < 0.001$), and excitation temperatures $T_{\rm ex}$ ($p < 0.001$), and lower virial parameters $\alpha_{\rm vir}$ ($p = 0.005$; see Section 4.3).

These findings are consistent with comparisons of YSOs and clumps in other low-Z regions. In the star-forming complex N159 in the LMC, for example, Nayak et al. (2018) found that CO clumps containing YSOs were more massive than clumps that did not contain YSOs, and that massive YSOs were typically associated with the most massive clumps. Similarly, in the LMC region N55, Naslim et al. (2018) observed that molecular cores containing YSOs possessed larger linewidths and masses than those that did not.

The majority of clumps (83 out of 110, or $\sim$75%) are not associated with any YSOs, but may have been in the past. We calculated the distance between each clump and its nearest YSO and found moderate negative correlations between distance to the nearest YSO and clump mass ($\rho_s = -0.48$, $p < 0.001$), and distance and σ_v ($\rho_s = -0.47$, $p < 0.001$). We estimated the distance that a clump could have plausibly traveled since formation of this generation of YSOs began 1–2 Myr ago (C11). The mean σ_v of all clumps is 0.48 km s^{-1} with a standard deviation of 0.17 km s^{-1}. Using this distribution of σ_v as a proxy for the speed at which clumps may be moving relative to each other, we calculated the distance traveled over a timescale of 1.5 Myr at a relative speed of 0.65 km s^{-1} to derive a potential distance traveled estimate of $\sim$1 pc. Twenty of the 83 clumps that do not contain YSOs have a YSO within this distance. From Mann-Whitney U-tests, these clumps have significantly larger σ_v than clumps outside

of this distance ($p = 0.002$, mean σ_v of 0.52 km s^{-1} versus 0.41 km s^{-1}).

Only five of the 33 YSOs (15%) are not embedded within the projected 2D boundaries of a clump, so traditional hypothesis testing to compare the properties of YSOs within clumps to YSOs outside of clumps is not appropriate. A simple comparison of the median masses of the two groups suggests that YSOs inside clumps are more massive than YSOs outside of clumps (median $M = 3.4\,M_\odot$ versus 2.3 $M_\odot$) and have higher envelope $\dot{M}$ accretion rates (median $\dot{M} = 2.1 \times 10^{-6}\,M_\odot$ yr^{-1} versus $\dot{M} = 0.76 \times 10^{-6}\,M_\odot$ yr^{-1}). This suggests that the YSOs not embedded within clumps are currently less actively accreting material; although, as discussed in Section 2.2, this fitted value is a limited indicator of the actual historical accretion rate of the objects.

We also checked if CO emission that was not assigned to a clump by the quickclump algorithm was present around seemingly isolated YSOs by stacking CO spectra around each YSO within an area equal to three synthesized beams. We found no robust evidence for strong CO emission around these YSOs (Y198, Y271, Y283, Y290, and Y358) with all YSOs having one or fewer 3σ detections in ^{12}CO and ^{13}CO out of the 105 channels in the stacked spectra.

Seale et al. (2012) found that a large number of massive YSOs in four LMC GMCs were not associated with any molecular clumps detected with HCO$^+$, which they suggested to be the result of the disruption of clumps on $\lesssim 1$ Myr timescales. In the 30 Doradus region of the LMC, Nayak et al. (2016) found that massive YSOs were more likely to be associated with CO clumps than their low-mass counterparts and concluded that the less-massive YSOs not associated with clumps were likely more evolved than the embedded YSOs, as they would have had sufficient time to dissipate their natal molecular clumps through UV radiation. We draw similar conclusions that unassociated YSOs may be more evolved than embedded YSOs, and that feedback from YSOs may affecting be the molecular gas on the scale of individual clumps ($\lesssim 1$ pc). We note, though, that the small sample sizes involved weaken the power of these conclusions, as do the large uncertainties on the masses and accretion rates of each individual YSO.

3.3.2. PMS Stars

G12 analyzed the spatial distribution of PMS stars in N90 and identified 14 subclusters. We supplement this work using the DBSCAN algorithm (Density-Based Spatial Clustering of Applications with Noise; Ester et al. 1996), a nonparametric clustering method that defines clusters as regions of high density separated by regions of low density. It requires the assignment of two parameters: the minimum number of points to form a cluster, MinPts, and the maximum distance over which two points can be considered neighbors, ϵ. We set the minimum number of cluster members as MinPts = 15 stars. Following Rahmah & Sitanggang (2016), we found the optimal value of ϵ by creating a nearest-neighbors graph of the distance between the $k =$ MinPts nearest-neighbors of points in ascending order and identifying the approximate point of maximum curvature. This yielded $\epsilon = 4.4''$.

We identified eight distinct clusters of PMS stars, the locations of which are shown in Figure 9 and properties of which are summarized in Table 1. Like G12, we find overdensities of PMS stars in the central NGC 602 association
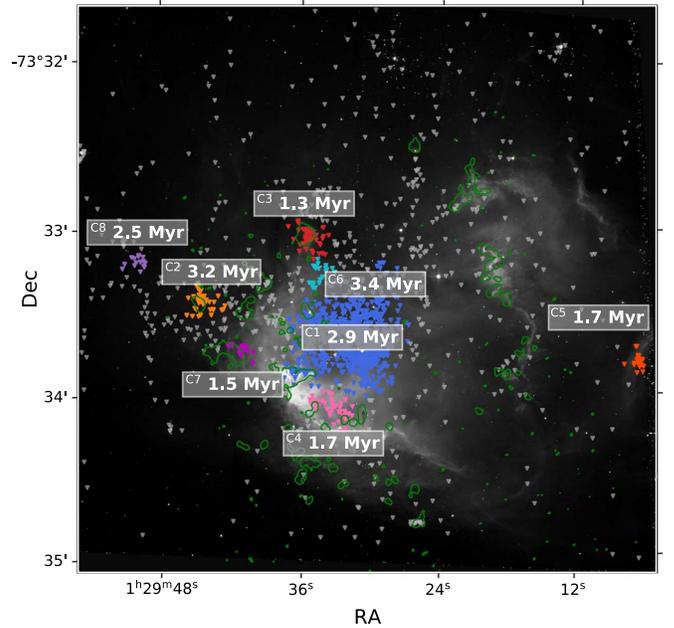

Figure 9. Locations of the PMS star clusters identified by the DBSCAN algorithm. PMS stars are marked with triangles. The clusters are denoted by color, and are labeled with their Table 1 ID numbers and the mean ages of their members. Nonclustered PMS stars are marked with gray triangles. The Hα image is in gray, and contours of integrated ^{12}CO(2–1) emission at 0.25 Jy beam^{-1} (km s^{-1})$^{-1}$ are shown in green.

Table 1
Properties of PMS Star Clusters

ID	R.A. (°)	Decl. (°)	N_{PMS}	Mean Age (Myr)	σ_{Age} (Myr)
C1	22.382	−73.561	779	2.9	1.6
C2	22.436	−73.557	49	3.3	1.4
C3	22.398	−73.551	44	1.9	1.9
C4	22.389	−73.568	41	1.8	1.5
C5	22.278	−73.563	27	2.0	1.9
C6	22.394	−73.554	22	3.2	1.8
C7	22.422	−73.562	21	2.0	1.9
C8	22.459	−73.553	15	3.5	1.3

Note. The reported position of each cluster is the mean position of all cluster members. N_{PMS} is the number of stars per cluster.

and along the rim of the H II region. The largest cluster, Cluster 1, is centered around NGC 602 and consists of 779 members (~50% of the total PMS sample). Oskinova et al. (2013) analyzed Chandra and XMM-Newton observations of N90 and found evidence for extended X-ray emission around this central cluster, and also in a feature on the rim directly to the north of NGC 602 where the DBSCAN algorithm identifies Cluster 3. They attributed these features to the effects of many low-mass PMS stars and YSOs unresolved in the X-ray data, which is consistent with the high concentration of resolved PMS stars in these locations that we find here.

Through the isochrone fitting described in Section 2.2 and shown in Figure 5, we find that the majority of the PMS stars in N90 are consistent with ages less than 5 Myr, with a mean age of 3 Myr. We note that the uncertainties on these estimates are largely due to the simple method of isochrone matching that we adopted. Cluster 1 has a mean age of ~3 Myr, which is

consistent with the age estimated for PMS stars in NGC 602 by C11 and G12. Clusters 3, 4, and 7 are scattered along the H II rim and possess slightly lower mean ages of ~2 Myr. This would seemingly support a star formation history in which the formation of these clusters was triggered by the formation of Cluster 1.

However, in all clusters, the dispersions in member age are large (typically $\gtrsim 1.5$ Myr). Additionally, there is a notable spread across V–I in the entire sample of PMS stars, with a handful of extremely young, red stars appearing to exist ($m_{555} - m_{814} \gtrsim 2.5$ mag). Visual inspection reveals that many of the reddest sources are located in extremely crowded areas (for example, Cluster 5 is at the edge of the HST coverage). These sources could be genuine, or could simply be a result of confusion or indicate the presence of misclassified asymptotic giant branch stars or unresolved background galaxies.

Many of the reddest sources are also associated with bright CO emission along the rim; this suggests that significant differential reddening could be resulting from the brightest clumps. Of the 1569 PMS stars, 130 fall within the projected boundaries of a CO clump. These sources appear significantly younger ($p < .001$ from a one-sided Mann-Whitney U-test, median age of 2 versus 3.5 Myr), i.e., redder, than PMS stars not inside CO clumps. Conversely, 40 of the 110 CO clumps contain at least one PMS star. Clumps that contain PMS stars have significantly higher masses ($p < 0.001$), surface densities ($p < 0.001$), and σ_v ($p = 0.003$) than clumps that do not contain PMS stars, and significantly lower virial parameters α_{vir} ($p < 0.001$; see Section 4.3).

Clusters 3 and 7 along the Hα rim (with apparent mean ages of 1.9 and 2.0 Myr, respectively) are both associated with strong CO emission. De Marchi et al. (2013) observed that the youngest and reddest PMS stars in N90 were located in dense areas of the rim, and suggested that if the extinction toward these stars was significantly higher than the rest of the sample ($A_V \simeq 2.25$ mag versus $A_V = 0.25$ mag), the ages of the outlier stars would be comparable to the ages of the PMS stars in the central NGC 602. In the N83 region of the SMC Wing, Lee et al. (2015) derived a relationship between CO intensity and extinction, $I_{CO}/A_V = 1.5$ K km s^{-1} (mag)$^{-1}$. The mean I_{CO} within clumps in N90 that contain PMS stars is 4.7 K km s^{-1}, which corresponds to $A_V \sim 3.1$ mag; a centrally embedded star might experience half of this value, $A_V \sim 1.6$ mag. Thus, reddening resulting from the CO clumps would be sufficient to cause Clusters 3 and 7 to appear much younger than they truly are. If this is the case, we would then find no strong evidence for a triggered star formation scenario.

Additionally, we find no correlation between age and radial distance from the center of NGC 602 in the full sample of PMS stars ($\rho_s = 0.08$, $p < 0.001$). The crossing time through the ~30 pc H II region is 3 Myr, which is equal to the mean ages of the entire PMS sample and most contained clusters. Since many of the PMS stars are located on the edges of the H II region, and the spatial distribution of their ages is roughly uniform, this suggests a sequential star formation scenario is more likely than a triggered event (i.e., the formation of local subclusters of PMS or OB stars would not have had time to directly influence the formation of other subclusters).

4. Molecular Gas and Star Formation in Low-metallicity Environments

4.1. Size–Linewidth–Surface Density Relationships

The relationship between size, linewidth, and surface density in molecular clouds has been extensively studied as a proxy for their dynamical states. Larson (1981) identified correlations between global cloud properties including size R, linewidth σ_v, and surface density Σ. The first of these correlations follows

$$\sigma_v = C\left(\frac{R}{1 \text{ pc}}\right)^\Gamma \text{ km s}^{-1}, \qquad (8)$$

with $\Gamma = 0.5$ and $C \simeq 0.72$ km s^{-1} pc$^{-0.5}$ (e.g., Solomon et al. 1987; Heyer et al. 2009, hereafter SRBY and H09, respectively). A virialized spherical clump described by a power-law density distribution $\rho \propto r^{-k}$ should additionally follow the relationship

$$\frac{\sigma_v^2}{R} = \frac{(3-k)}{3(5-2k)}\pi G\Sigma. \qquad (9)$$

Figure 10 compares σ_v, R, and Σ for the N90 clumps. We also show cores, clumps, and GMCs from:

1. two samples of Galactic GMCs observed by H09, with the first defined from SRBY's ^{12}CO GMCs, and the second from the half-power contours of the central GMCs cores observed in ^{13}CO (median radii R of 9.7 pc and 1.6 pc, respectively);
2. clouds in the Galactic center studied by Oka et al. (2001) in ^{12}CO (median R of 8.7 pc);
3. clouds in the Ophiuchus molecular cloud in ^{13}CO from Ridge et al. (2006; median R of 0.07 pc);
4. cores identified using the dendrogram algorithm within the Galactic molecular cloud Perseus A observed in ^{13}CO by Shetty et al. (2012; median R of 0.07 pc);
5. clumps in the Magellanic Bridge studied by Kalari et al. (2020) in CO (1–0; mean R of 1.1 pc);
6. clumps in the Magellanic Bridge studied in ^{12}CO (2–1) by Valdivia-Mena et al. (2020; mean R of 1.1 pc);
7. GMCs identified by Ochsendorf et al. (2017) in ^{12}CO in ~150 LMC star-forming regions (median R of 27 pc);
8. clumps identified by Wong et al. (2019) in ^{12}CO in the LMC regions 30 Doradus, A439, GMC 104, GMC 1, PCC, and N59C (median R of 1 pc); and
9. GMCs in the SMC and dwarf galaxy IC 10 observed in CO (2–1) and (1–0) by Bolatto et al. (2008; median R of 15 pc)

Figure 10(a) compares σ_v to R. The expected contribution to linewidth by thermal motion at $T = 20$ K, $\sigma_{v,th} \sim 0.08$ km s^{-1} is also shown. We fit a relationship for the N90 clumps of $\Gamma = 0.81 \pm 0.10$ and $C = 0.98 \pm 0.09$ km s^{-1}. Similarly steep values of Γ compared to SRBY have been derived in other low-Z, low-density regions throughout the SMC, LMC, and other local dwarf galaxies (with $\Gamma \sim 0.55$–0.85 and $C \sim 0.2$–0.6 km s^{-1}; Bolatto et al. 2008; Hughes et al. 2010, 2013; Wong et al. 2019; Finn et al. 2022). Our fit C is significantly higher than that derived in these studies, suggesting that the clumps in N90 have larger linewidths at a given size than structures in those other dwarf galaxy regions.
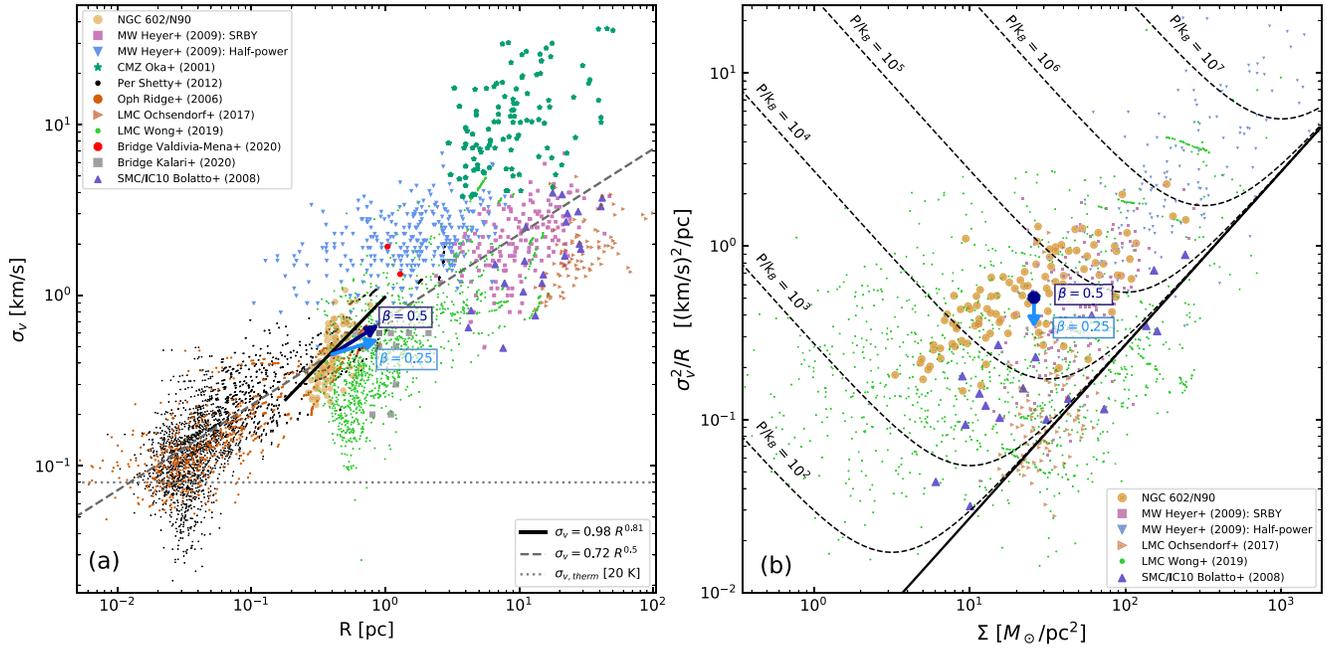
Figure 10. Size–linewidth–surface density plots, adapted from O'Neill et al. (2022) with the addition of N90 clumps. (a) Velocity dispersion σ_v compared to radius R of clumps from studies described in Section 4.1. The arrows show the corrections needed to account for CO-dark gas on observable CO clump properties for a typical clump with $[R_{CO} = 0.40$ pc, $M(R_{CO}) = 13\ M_\odot$, $\sigma_v(R_{CO}) = 0.45$ km s$^{-1}]$. The arrows move from the properties of the observed CO clump to the inferred full state of the clump including CO-dark gas. The dark blue arrow follows a velocity profile $\sigma_v \propto R^{0.5}$ [$\beta = 0.5$], and the light blue arrow follows a velocity profile $\sigma_v \propto R^{0.25}$ [$\beta = 0.25$]. Both arrows show the effect for a density profile $\rho \propto R^{-1}$ [$k = 1$] and $f_{DG} \sim 0.8$. The gray dashed line follows the relationship $\sigma_v = 0.72R^{0.5}$ derived by SRBY, and the gray dotted line is the expected σ_v at $T = 20$ K from thermal motion. The black solid line was fit to the N90 clumps and follows $\sigma_v = 0.98\ R^{0.81}$. (b) Size–linewidth parameter σ_v^2/R compared to surface density Σ, with correction arrows as in (a). The black line corresponds to virial equilibrium (Equation (9) with $k = 0$), and the black curves correspond to virial equilibrium under varying degrees of external pressure (with units of P/k in K cm^{-3}, Equation (11) with $\Pi = 0.6$).

Kepley et al. (2016) studied eight GMCs in the low-Z ($Z \sim Z_{SMC}$) starburst dwarf galaxy II Zw 40 and derived similarly high C; they attributed this to high linewidths and surface densities stemming from a merger between dwarf galaxies that triggered the starburst, rather than high external pressure supporting the GMCs against collapse. Imara & Faesi (2019) identified ∼120 GMCs in the moderately low-Z ($Z \sim 0.7Z_\odot$) starburst dwarf galaxy He 2–10, and found both higher velocity dispersions, surface densities, and C than in comparable Milky Way clouds. They also fit a very steep size–linewidth slope of $\Gamma = 1.3$, which they suggested could be the result of tidal interactions or energy and momentum injected from nearby superstar clusters.

Figure 10(b) compares surface density Σ to the size–linewidth parameter $[\sigma_v^2/R]$. Virialized clumps are expected to follow Equation (9), but the N90 clumps have higher σ_v^2/R's for a given Σ than would be expected based on from this trend. A likely reason that clumps in a region would deviate from expected trends in size–linewidth space, and have higher kinetic energy at a given size scale, is the OB stars in the center of NGC 602 are injecting kinetic energy into the surrounding gas.

If there is significant inter-cloud thermal pressure acting on the molecular clumps, as observed by Oka et al. (2001) in the Galactic center, and the clumps are assumed to be in virial equilibrium with that pressure, turbulence can be treated as a pressure term (Field et al. 2011). This increase in internal turbulent pressure would then be reflected as higher linewidths than expected, as observed in the relationship between σ_v^2/R and Σ in clumps in N90. The external pressure P_e for a clump to remain bound (under the assumption that they are virialized, which is discussed in Section 4.3) can be found using

(Elmegreen 1989),

$$P_e = \frac{3\Pi M \sigma_v^2}{4\pi R^3}. \tag{10}$$

The median external pressure required for clumps to remain bound is $P_e/k_B \sim (2.4 \pm 1.3) \times 10^4$ K cm^{-3}. Clumps on the rim require, on average, $1.5 \times$ larger external pressures to remain bound than clumps that are not on the rim, but a K-S test reveals no overall significant difference between the distributions of the two groups ($p = 0.14$).

The surface density Σ and size–linewidth parameter σ_v^2/R for clumps in pressure-bounded virial equilibrium can be related to P_e as (Field et al. 2011),

$$\frac{\sigma^2}{R} = \frac{1}{3}\left(\pi\Pi G\Sigma + \frac{4P_e}{\Sigma}\right). \tag{11}$$

We adopt $\Pi = 0.6$ for a uniform sphere (Field et al. 2011). These relationships are represented in Figure 10(b) by the black V-shaped curves for P_e/k_B between 10^2–10^7 K cm^{-3}. The N90 clumps do not appear consistent with being supported by any one value of P_e, but the majority of the clumps require between $P_e = 10^3$ and 10^6 K cm^{-3}.

The clumps identified by Wong et al. (2019) in six GMCs in the LMC with ^{12}CO and ^{13}CO emission were observed at comparable angular resolution to our data (having a synthetic beam size of 3″5 [0.8 pc], versus 1″3 [0.4 pc] in the data we present here). They found higher σ_v at a given R in regions with higher infrared surface brightness (a plausible measure of SFR and stellar feedback). The mean 8 μm brightness of ∼0.5 MJy sr^{-1} in N90 corresponds to the lower end of surface

brightnesses in the Wong et al. (2019) study of LMC regions. Thus, N90 is consistent with the Wong et al. (2019) findings in this parameter space, although care should be exercised since both measures may be affected by reduced metallicity. The 8 μm diffuse emission at a given radiation intensity is lower in the SMC than in LMC, and the CO measurements may also be affected, as discussed below.

4.2. "CO-dark" Gas: Effects of Low Metallicity on CO Diagnostics in N90

At low metallicities, reduced dust-to-gas ratios and typically stronger radiation fields increase the efficiency of CO destruction (Madden et al. 2006; Gordon et al. 2011; Madden et al. 2020) and decrease the effectiveness of CO as a tracer for H_2. The $C^+/C^0/CO$ transition retreats farther into the center of clumps, which causes the fraction of "CO-dark" H_2 gas mass not traced by CO to increase (Wolfire et al. 2010; Glover & Mac Low 2011). It is possible that the discrepancies in N90 clump properties compared to expected size–linewidth–surface density trends are the result of this increased proportion of CO-dark gas. We apply corrections derived by O'Neill et al. (2022, hereafter O22) to account for the expected contribution of CO-dark gas on observed clump properties in N90.

As defined by Wolfire et al. (2010), the fraction of H_2 gas mass that is CO-dark in a clump, f_{DG}, can be expressed as

$$f_{DG} = 1 - \frac{M(R_{CO})}{M(R_{H_2})}, \qquad (12)$$

where $M(r)$ is the mass contained within a given radius r, R_{CO} is the radius of the CO-traceable material, and R_{H_2} is the radius at which half of the hydrogen in the clump's diffuse envelope is molecular and half is atomic. Under typical Galactic conditions, f_{DG} is found to be $\gtrsim 0.3$ (e.g., Grenier et al. 2005; Abdo et al. 2010; Velusamy et al. 2010; Lee et al. 2012; Langer et al. 2014; Xu et al. 2016).

To apply the corrections derived by O22, we assume that clumps follow a power-law density profile with $k = 1$ (Equation (6)) and internal velocity dispersion profile, $\sigma_v(r)$, of

$$\sigma_v(r) = \left(\frac{r}{R_{CO}}\right)^\beta \sigma_v(R_{CO}). \qquad (13)$$

$\beta \sim 0.2$–0.3 is common in observations and simulations of young cores and clumps (Caselli & Myers 1995; Tatematsu et al. 2004; Lee et al. 2015; Lin et al. 2022), while a steeper $\beta \sim 0.5$ in alignment with the global size–linewidth relationship of SRBY with $\Gamma = 0.5$ (Equation (8)) has been found to hold on larger scales (e.g., Heyer & Brunt 2004; Dobbs 2015). Based on these findings, we adopt $\beta = 0.25$ for the bulk of our analysis, but also present results for $\beta = 0.5$.

We estimate an appropriate f_{DG} for N90 based on measurements of CO-dark gas content in other low-Z, low-density environments. In the LMC, Chevance et al. (2020) derived $f_{DG} \gtrsim 0.75$ in the star-forming region 30 Doradus, and in the H II region N11, Lebouteiller et al. (2019) found that the majority (40%–100%) of molecular gas was CO-dark. Throughout the low-Z outskirts of the Milky Way, Pineda et al. (2013) derived $f_{DG} \sim 0.8$, while in the nearby low-metallicity dwarf galaxy NGC 4214 ($Z \sim 0.3$–0.4 $Z_\odot$; Hermelo et al. 2013), Fahrion et al. (2017) derived $f_{DG} = 0.79$. Pineda et al. (2017) found that 77% of the total molecular gas in their

sample of 18 line-of-sight pointings across the SMC was CO-dark H_2, and in the SMC regions, N66, N25+N26, and N88 (located in the northern Bar, southwest Bar, and Wing, respectively). Requena-Torres et al. (2016) derived a typical fractional abundance of CO-dark gas to be 80%–95%. In four star-forming regions in the nearby southwest Bar of the SMC (where cloud density is comparable to N90 and the Wing; $\bar{N} \lesssim 2 \times 10^{21}$ cm^{-2}), Jameson et al. (2018) derived an average $f_{DG} \simeq 0.8$. Based on these results, we adopt $f_{DG} \sim 0.8 \pm 0.1$ for an estimated dark-gas fraction in N90 for the remainder of this work.

O22 derived corrections for clump properties under a power-law density profile, including

$$
\begin{aligned}
R_{H_2} &= [1 - f_{DG}]^{1/(k-3)} R_{CO}, \\
\sigma_v(R_{H_2}) &= [1 - f_{DG}]^{\beta/(k-3)} \sigma_v(R_{CO}), \\
M(R_{H_2}) &= [1 - f_{DG}]^{-1} M(R_{CO}), \\
\Sigma_{H_2} &= [1 - f_{DG}]^{(1-k)/(k-3)} \Sigma_{CO}.
\end{aligned} \qquad (14)
$$

After applying these corrections to the $M_{X_{CO,B}}$-derived clump masses, which estimate the mass within the CO-traced regions, we find a total molecular gas mass in N90 of $M_{DG} \sim 16{,}600 \pm 2400\ M_\odot$. The errors on this estimate are derived from the combined uncertainties of f_{DG} and $M_{X_{CO,B}}$.

In Figures 10(a) and (b), we demonstrate the effects of these corrections on a typical observed clump with properties [$R_{CO} = 0.40$ pc, $M(R_{CO}) = 13\ M_\odot$, $\sigma_v(R_{CO}) = 0.45$ km s^{-1}, $\Sigma_{CO} = 26\ M_\odot$ pc^{-2}]. The arrows show the change in placement in size–linewidth–surface density space from the example clump's observed CO properties to its inferred "true" characteristics when including CO-dark gas for $\beta = 0.25$ and $\beta = 0.5$. Assuming $f_{DG} = 0.8$ and $k = 1$, the preferred $\beta = 0.25$ yields corrected properties of [$R_{H_2} = 0.9$ pc, $M(R_{H_2}) = 65\ M_\odot$, $\sigma_{v,H_2} = 0.55$ km s^{-1}, $\Sigma_{H_2} = 26\ M_\odot$ pc^{-2}]. In this case, the corrections bring clump properties closer to agreement with expected Σ–[σ_v^2/R] trends. Since this change is only by a relatively small amount, though, and O22 demonstrated that the effects of these corrections vary significantly depending on the density and velocity profiles assumed, we conclude that it is unlikely but not impossible that enhanced photodissociation in this low-Z environment is responsible for observed departures from size–linewidth–surface density trends in N90.

4.3. Stability of Clumps

The evolution and stability of clumps can be also studied through assessing their virial masses, which for a clump with a power-law density profile (Equation (6)) can be found as (Solomon et al. 1987; MacLaren et al. 1988)

$$M_{vir}(r) = \frac{3(5 - 2k)}{(3 - k)} \frac{r\ \sigma_v^2(r)}{G}, \qquad (15)$$

where k is the index of the power law. As in Section 4.2 we assume $k = 1$. Virial masses for clumps in N90 ranged from $16\ M_\odot$ to $620\ M_\odot$, with a median mass of $85\ M_\odot$ and total virial mass of all clumps of $14{,}045 \pm 515\ M_\odot$.

We compare the relationship between individual M_{vir} and $M_{X_{CO,B}}$ in Figure 11. A relationship $M_{vir}/M \propto M^{-\eta}$ has been observed to hold for dense clumps in many regions, with estimates of η typically ranging from $\eta \sim 0.3$–0.4 in Galactic clouds (e.g., Yonekura et al. 1997; Ikeda et al. 2009).
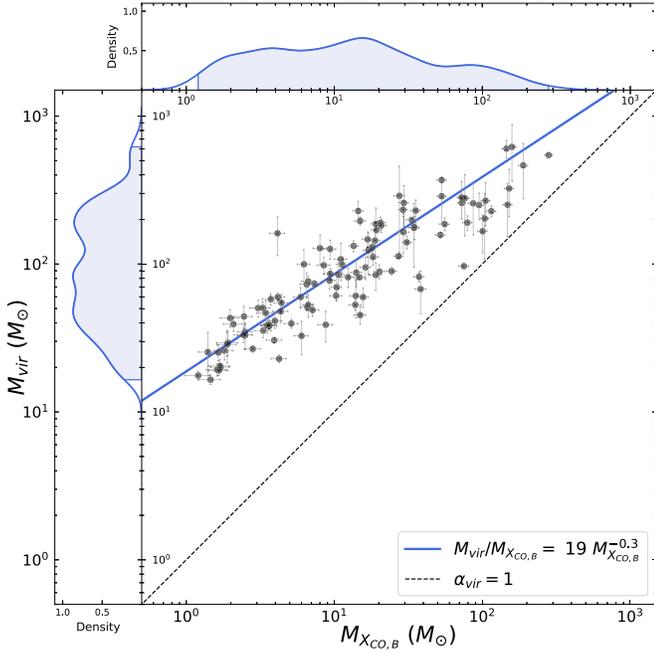
Figure 11. Clump virial mass M_{vir} is compared to clump $X_{CO,B}$-derived mass $M_{X_{CO,B}}$. The black dashed line shows a 1:1 relationship where $M_{vir} = M_{X_{CO,B}}$, i.e., where the virial parameter $\alpha_{vir} = 1$ and stability could be expected, and the blue line shows a best-fit relationship $M_{vir}/M_{X_{CO,B}} = 19\,M_{X_{CO,B}}^{-0.34}$. The two mass distributions are represented individually by Gaussian KDEs placed horizontally on the top axis of the scatter plot ($M_{X_{CO,B}}$) and on its left axis (M_{vir}).

A least-squares fit for clumps in N90 yields $M_{vir}/M_{X_{CO,B}} = (18.8 \pm 1.3)\,M_{LTE}^{(-0.34\pm0.04)}$. KDEs of the distributions of M_{vir} and $M_{X_{CO,B}}$ are also shown, with M_{vir} being centered at higher masses than $M_{X_{CO,B}}$.

We then calculated the virial parameter α_{vir} defined by Bertoldi & McKee (1992) for all clumps as

$$\alpha_{vir} = \frac{2\Omega_K}{|\Omega_G|} = \frac{M_{vir}}{M_{X_{CO,B}}}, \qquad (16)$$

where Ω_G is the total gravitational potential energy, and Ω_K is the total kinetic energy. $\alpha_{vir} \sim 1$ indicates that a clump is gravitationally stable, and $\alpha_{vir} \gg 1$ indicates that a clump is subcritical and will likely expand unless confined by external pressure. There is a wide variation in α_{vir} from clump to clump, with α_{vir} ranging from 1.3 to 39. The median value is $\alpha_{vir} = 7.95$, with lower and upper quartiles of 4.4 and 11.5, respectively.

This is significantly higher than many recent measurements of $\alpha_{vir} \lesssim 2$ in molecular clouds (see Kauffmann et al. 2013 for a review), and may be an overestimate due to the effects of CO-dark gas, which we discuss below. In the 30 Doradus region of the LMC, Wong et al. (2017) found that virial clump masses were typically an order of magnitude larger than CO-derived masses, which is similar to what we observe here. Schruba et al. (2017) studied ~150 small CO clumps (mean radius $R \simeq 2.3$ pc) in five star-forming regions in the $Z = 1/5\,Z_\odot$ dwarf galaxy NGC 6822 and found large values of α_{vir} (from ~1 to $\gtrsim$10). Similarly high values of α_{vir} have also been found in clumps in the Galactic Central Molecular Zone (Myers et al. 2022) and in cores in the Pipe Nebula (Lada et al. 2008).

The increased degree of photodissociation in low-Z environments (see Section 4.2) compromises the fundamental assumption that CO emission accurately traces clump mass, and by extension interpretations of α_{vir} values. We expect the enhanced amount of CO-dark gas in this region to cause $M_{X_{CO,B}}$ to be a significant underestimate of the total amount of molecular gas (Section 4.2), so correcting for the "true" values of α_{vir} including CO-dark gas could bring the clumps more in line with expected trends. O22 derived the CO-dark-corrected virial mass and parameter as

$$M_{vir}(R_{H_2}) = [1 - f_{DG}]^{(2\beta+1)/(k-3)}\,M_{vir}(R_{CO}),$$
$$\alpha_{vir,H_2} = [1 - f_{DG}]^{(2\beta+k-2)/(k-3)}\,\alpha_{vir,CO}. \qquad (17)$$

We correct clump virial masses and parameters using Equations (14) and (17), with a CO-dark gas mass fraction $f_{DG} \sim 0.8$ assumed in Section 4.2 and velocity dispersion profiles following $\beta = 0.25$ and $\beta = 0.5$. For [$k = 1$, $\beta = 0.5$], values of α_{vir} remain unchanged from the original estimate. For the preferred [$k = 1$, $\beta = 0.25$], the new median value is $\alpha_{vir,H_2} = 5.3$. Although this is a reduction, this is still much higher than would be expected for a virialized clump.

We note that the calculations of virial masses suffer from large uncertainties stemming from the determination of radii and assumption of a spherical clump, and that the many uncertainties in the calculations of column densities (especially those stemming from assuming equal excitation temperatures for ^{12}CO and ^{13}CO and constant abundance ratios between ^{12}CO, ^{13}CO, and H$_2$), $X_{CO,B}$ masses, and the dark-gas mass fraction are also significant. Still, the only marginal decrease in α_{vir} implies that the clumps are either confined by high levels of external pressure or are not evolving near a virialized state. In any case, it is unlikely that CO-dark gas is responsible for the observed high α_{vir}.

The high values of α_{vir} suggest that the clumps have higher internal kinetic energies than clumps in other regions and galaxies. If the clumps are long-lived, this imbalance must be addressed by external pressure or magnetic fields. The data are generally consistent with N90 being an energetic region and contributing a higher inter-clump-medium pressure than in more quiescent regions. If the central OB cluster is responsible for this energetic state, we would expect to see some variation in virial parameter and other clump properties with proximity to the cluster.

However, we found no significant difference in the distributions of α_{vir} between the rim versus nonrim clumps ($p = 0.095$ from a K-S test). As shown in Figure 12, there is no correlation between α_{vir} and distance from NGC 602 for clumps on the Eastern rim ($\rho_s = 0.04$, $p = 0.7$), while on the Western rim, there is only a moderate trend for increased α_{vir} as a function of distance from Sk 183 ($\rho_s = 0.46$, $p = 0.006$). This is similar to the recent results of Wong et al. (2022) and Finn et al. (2022) in the LMC, who both found no significant correlations between clump α_{vir} and distance from the super star cluster R136. The overall absence of any strong trends with position in N90 suggests that the entire region is energetic for a different reason, e.g., the aftereffects of the collision between the H I clouds/supershells.

4.4. Efficiency of Low-Z Star Formation

The supergiant shell SGS 1 falls on the boundary between the H I-dominated outskirts and molecule-rich center of the SMC, and the SFR per unit area and mass has been observed to
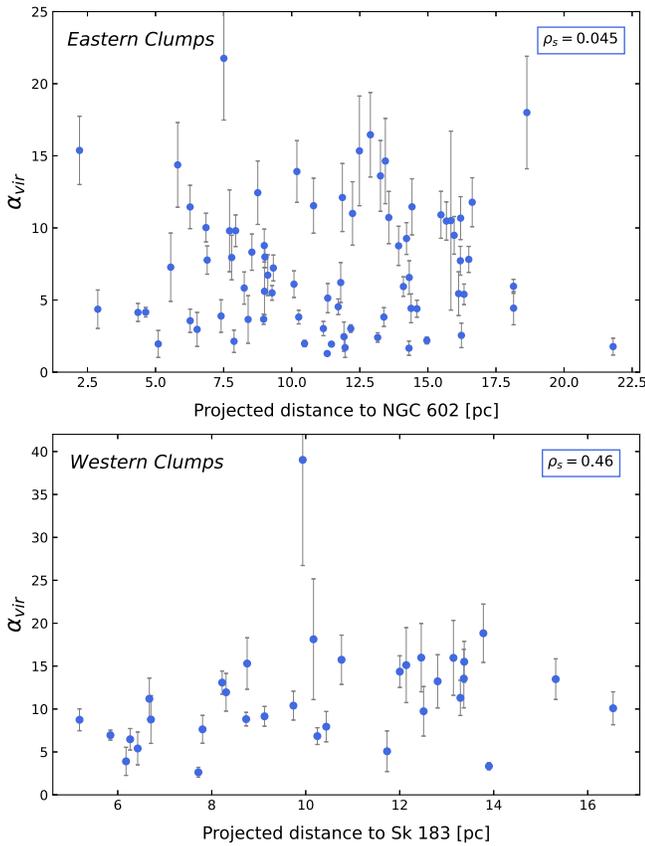
Figure 12. Top: the virial parameter $\alpha_{\rm vir}$ is compared to projected distance to NGC 602 for clumps in the eastern half of N90. The value of Spearman's ρ_s rank correlation coefficient for the two variables is shown in the top right. Bottom: the same as the top, but for projected distance to the massive star Sk 183 for clumps on the western half of N90.

drop dramatically along such transitions (Krumholz 2013). The low amount of CO emission to the south of N90 compared to the concentrated CO emission to its north may reflect this transition in the Wing. When gas mass is assessed using CO emission, low-Z environments have been observed to have higher SFRs, and by extension higher apparent star formation efficiencies (SFEs) than higher-Z regions (e.g., Galametz et al. 2009; Schruba et al. 2012, 2017), although this may simply be the result of CO being a poor tracer of H_2 at low Z. Here we explore metrics of SFE in N90.

We initially examined the SFE in N90 at the scale of individual clumps ($\lesssim 1$ pc). If one calculates a by-clump efficiency as the ratio of the mass of any contained YSOs to CO-dark corrected clump mass, efficiency appears to decrease with clump mass, with values ranging from 0.5%–16.5%; however, this ratio cannot account for the unknown difference between the original clump mass that created a given YSO and the observable extant gas mass. Since the gas within a few parsecs of a YSO is quickly disrupted by the star formation process, and the dynamic range of the Spitzer-identified YSO masses is small, it is difficult to conclude much from such a clump-scale efficiency.

Although the offset in time between current and original gas mass is an unavoidable limitation of SFE measurements, comparing the total YSO and CO masses is more useful in that it likely averages over a significant portion of the clump evolutionary sequence. It can then provide a more meaningful

efficiency estimate than analysis of individual clumps. With this in mind, we studied SFE and the SFR throughout the entirety of N90 through analyzing the overall population of candidate YSOs.

To account for incompleteness in the YSO sample, we assumed a two-part stellar initial mass function (IMF) of the form $dN/d\log M \propto M^{-\alpha}$, where $\alpha = 0.3$ below 0.5 $M_\odot$ and $\alpha = 1.3$ above 0.5 $M_\odot$ (Kroupa 2001). We found no high-mass YSOs ($\gtrsim 10$ $M_\odot$), which suggests that the IMF for the current generation of star formation in N90 is not fully populated. We scaled this mass function to the peak of our observed YSO mass distribution at 3 $M_\odot$ and integrated over 0.08 to 50 $M_\odot$ to derive a total YSO mass in N90 of $M_* \simeq 1250 \pm 160\,M_\odot$, which corresponds to an estimated total number of YSOs of $N({\rm YSO}) \simeq 260$.

In comparison, C11 derived a total YSO mass of 2250 $M_\odot$ as inferred through the same method. This difference stems from our globally lower YSO mass estimates. Our list of YSO candidates is identical to C11's but (all but one of the) revised individual YSO masses are lower than the original estimates, so the peak of our stellar mass function is shifted to lower masses than C11's. Since C11 and this work both infer the total YSO mass through scaling a Kroupa (2001) IMF to the peak of the YSO mass function, it is unsurprising that we derive a significantly lower total mass estimate.

Using only the $X_{\rm CO,B}$-derived CO-bright gas mass, this total YSO mass yields a recent SFE ($\epsilon = M_*/M_{\rm gas}$) in N90 of $\epsilon_{X_{\rm CO,B}} = 38\% \pm 7\%$. After correcting for CO-dark gas, we estimate an overall $\epsilon_{\rm DG} = (1 - f_{\rm DG})\epsilon_{X_{\rm CO,B}}$ (O22) of $\epsilon_{\rm DG} = 8\% \pm 3\%$. This estimate is significantly lower than the 20% formation efficiency estimate that Fukui et al. (2020) derived for N90, which is unsurprising due to our addition of CO-dark gas mass to our calculation.

We calculated the SFR in N90 as $\mathrm{SFR}_{\rm YSO} = N({\rm YSOs}) \times \bar{M}/t_*$ (Ochsendorf et al. 2017), where $\bar{M}$ is the mean mass of the fully populated IMF (here 0.5 $M_\odot$), and t_* is the typical YSO age (here 1 Myr). We derived an $\mathrm{SFR}_{\rm YSO} = 130 \pm 30\,M_\odot$ Myr^{-1}. From studying the optical PMS population in N90, Cignoni et al. (2009) found that the SFR has been increasing over the last 10 Myr, with an SFR of 150 $M_\odot$ Myr^{-1} between 5 and 2.5 Myr ago and reaching a peak of 300–700 $M_\odot$ Myr^{-1} in the last 2.5 Myr. C11 derived an SFR of 2200 $M_\odot$ Myr^{-1} over the last 1 Myr through analyzing the YSO mass function; we attribute our reduced estimate to our globally lower fitted YSO masses discussed earlier in this subsection.

We then derived the SFE using the notation of Kennicutt & Evans (2012) where $\epsilon' = \mathrm{SFR}/M_{\rm gas}$. Using the $X_{\rm CO,B}$ CO-bright mass estimate, we estimate that $\epsilon_{X_{\rm CO,B}}' = 0.04 \pm 0.01$ Myr^{-1}, while the CO-dark corrected mass estimate yields $\epsilon_{\rm DG}' = 0.01 \pm 0.005$ Myr^{-1}. If the SFRs derived by Cignoni et al. (2009) or C11 were used, ϵ' would increase by a small amount, but would not change the conclusions we draw below.

In Figure 13, these results are compared to values derived for ~ 150 star-forming regions in the LMC through analysis of YSO mass functions by Ochsendorf et al. (2017) and for a sample of ~ 190 Galactic clouds analyzed by Lee et al. (2016). Ochsendorf et al. (2017) and Lee et al. (2016) both found that ϵ' increased with decreasing cloud masses. For comparison, we also derive an estimated ϵ' for SGS 1. Rubele et al. (2018) derived an SFR of $\sim 1.19 \times 10^{-3}\,M_\odot$ yr^{-1} in the last 8 Myr for

Table 2
History of N90

| Time	Event and Derivation Method	Reference
	Older Populations Form in SGS 1	
$\gtrsim$100 Myr	SF begins in SGS 1, from SED and HRD fitting	Ramachandran et al. (2019)
$\sim$50 Myr	Subclusters NGC 602 B and NGC 602 B2 form, from optical CMD fitting	De Marchi et al. (2013)
25–40 Myr	Extended SF event in SGS 1, from optical/near-UV CMD fitting	Fulmer et al. (2020)
	Formation Event for NGC 602	
8 Myr	Collision between clouds, from separation in H I velocity components	Fukui et al. (2020)
7 Myr	Collision between shells, from expansion velocities of H I shells	Nigra et al. (2008)
	SF Begins in Central Cluster NGC 602	
$\lesssim$5 Myr	Central PMS stars form, from optical CMD fitting	Gouliermis et al. (2012)
2–4 Myr	Central OB and PMS stars form, from optical CMD fitting	Carlson et al. (2011)
	Subsequent SF in N90	
2.5 Myr	Maximum SF rate reached, from optical PMS population	Cignoni et al. (2009)
$\lesssim$2.5 Myr	PMS stars form in subclusters along rim, from optical CMD fitting	Gouliermis et al. (2012)
2 Myr	Median apparent age of PMS stars in CO clumps, from optical CMD fitting	This work
1–2 Myr	Ongoing intermediate-mass SF, from SED fitting of YSOs	This work
<1–2 Myr	YSOs form, from SED fitting of evolutionary phase	Carlson et al. (2011)
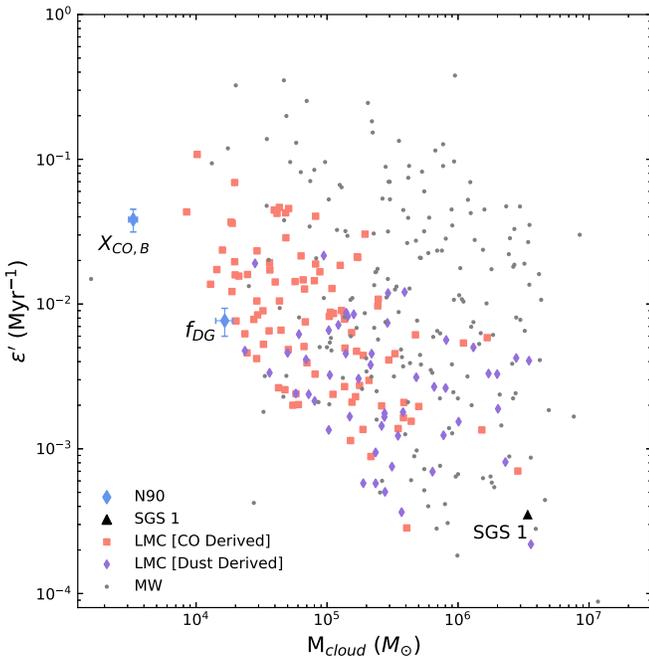
Figure 13. Star formation efficiency (SFE) $\epsilon' = \mathrm{SFR}/M_{\mathrm{cloud}}$ is compared to cloud mass M_{cloud}. The ϵ' value we derived from the CO-bright gas mass in N90 using an $X_{\mathrm{CO,B}}$ conversion factor ($X_{\mathrm{CO,B}} = 3.4 \times 10^{20}$ cm^{-2} (K km s^{-1})$^{-1}$) is shown along with the ϵ' derived through correcting for CO-dark gas mass ($f_{\mathrm{DG}} \simeq 0.8$; Section 4.2) by the labeled blue points. The ϵ' we derived for SGS 1 is marked with a black diamond. Results for a sample of LMC GMCs analyzed by Ochsendorf et al. (2017) are shown: pink squares had masses derived through α_{CO} conversion, and purple diamonds had masses derived from Jameson et al.'s (2016) dust-based molecular hydrogen map of the LMC. A sample of Galactic clouds studied by Lee et al. (2016) is also shown by gray circles.

a $21' \times 21\overset{'}{.}5$ region centered in SGS 1. We assume a typical N(H I) in this area of 2×10^{21} cm^{-2} (Welty et al. 2012) and a mean atomic mass of $\bar{m} = 1.5 m_{\mathrm{H}}$ (Nigra et al. 2008). This yields an estimated gas mass within the Rubele et al. (2018) region of $3.4 \times 10^6 \, M_\odot$ and an $\epsilon' = 3.5 \times 10^{-4}$ Myr^{-1}, which is significantly lower than the values derived in N90 and consistent with decreasing ϵ' with increasing gas mass.

However, on the low end of values observed for similar LMC and Galactic clouds, the SFE we derive for the relatively low-mass N90 is consistent with this trend. We therefore conclude that star formation in N90 and this region of the Wing of the SMC is not significantly more efficient than in higher-Z environments.

5. Discussion and Conclusions

5.1. Evolutionary History of N90

We review the scenarios for the formation of N90 presented in previous studies in Table 2, and add the results of this work. A combination of stimulated and stochastic star formation in this region of the SMC Wing has been ongoing for at least 100 Myr, with a notable extended star formation event between 25 and 40 Myr ago (Ramachandran et al. 2019; Fulmer et al. 2020). Between 7 and 8 Myr ago, a collision occurred between $\sim$500 pc components of H I within the supergiant shell now identified as SGS 1 (Nigra et al. 2008; Fukui et al. 2020). Turbulence and compression stemming from this collision triggered the formation of NGC 602 3–5 Myr ago (Carlson et al. 2011; Gouliermis et al. 2012) and subsequent creation of the H II region N90. The parsec-scale CO clumps to the north of N90 may retain signatures of the H I collision in the form of inflated excitation temperatures and column densities, but determining whether a collision between shells (Nigra et al. 2008) or clouds (Fukui et al. 2020) is more likely to be responsible is not yet possible.

Intermediate-mass YSOs have been forming along the H II rim over the last 1–2 Myr (Carlson et al. 2011), but it is unclear if this was triggered by the formation of the central cluster. There is very little variation in the ages of PMS stars with distance from NGC 602, and although some isolated clusters of young ($\lesssim$2 Myr) PMS stars appear to exist along the rim, they coincide with CO emission sufficiently strong to cause age underestimates by $\gtrsim$1 Myr. There is some evidence for YSOs disrupting their natal clumps on the parsec-scale, but on the scale of the entire region, there are very few significant correlations between clump properties and distance from NGC 602 or Sk 183. We conclude that a sequential star formation process, in which the creation of the central NGC 602 cluster

did not directly cause the formation of the YSOs or PMS stars along the rim, is more likely to be present than a triggered scenario.

5.2. Conclusions

We present results from ALMA observations of molecular gas in the low-metallicity star-forming region NGC 602/N90. The main conclusions of this analysis are as follows:

1. CO emission in N90 is confined to 110 subparsec-scale clumps arranged around the region's rim. Only 26% of clumps are traced by both ^{12}CO and ^{13}CO, with the remaining 74% of clumps only being traced by ^{12}CO with no strong corresponding ^{13}CO emission (Section 2.1.2). We derive a CO-to-H$_2$ conversion factor of $X_{CO, B} = (3.4 \pm 0.2) \times 10^{20}$ cm^{-2} (K km s^{-1})$^{-1} \simeq 1.7$ $X_{CO, MW}$ from the clumps that do possess strong emission in both ^{12}CO and ^{13}CO. Applying this factor to all clumps yields a total CO-traced mass of $3310 \pm 250\,M_\odot$ (Section 2.1.3).
2. We estimate a total molecular gas mass in N90 of $16{,}600 \pm 2400\,M_\odot$ through CO-dark gas mass correction (Section 4.2).
3. Clumps in N90 do not agree with expected trends in size–linewidth–surface density space, and have larger velocity dispersions and lower surface densities than predicted by relationships derived from Galactic clouds (Section 4.1). Additionally, CO-derived clump masses are significantly lower than virial masses, yielding high virial parameters (typical $\alpha_{vir} = 4$–11) and implying that clumps are either dispersing or confined by high levels of external pressure (Section 4.3). We use models of clumps with CO-dark gas to demonstrate that it is unlikely that CO-dark gas is responsible for either of these effects.
4. We refit Spitzer YSO candidates identified by Carlson et al. (2011) and find by including new mid-to-far-IR photometry that nearly all objects are less massive than previously estimated. Analysis of the present-day accretion rate of the YSO candidate reveals that intermediate-mass star formation has likely been occurring throughout N90 in the last 1–2 Myr (Section 3.3.1). Eighty-five percent of YSO candidates within the field observed by ALMA appear to be embedded within CO clumps. We derive a recent ($\lesssim 1$ Myr) SFR of $130 \pm 30\,M_\odot$ Myr^{-1}, with a total YSO mass of $1250 \pm 160\,M_\odot$ and CO-dark gas corrected SFE of $\epsilon \simeq 8\% \pm 3\%$ (Section 4.4).
5. We find no strong evidence that NGC 602 has directly triggered star formation along the rim of N90. Spatial position relative to NGC 602 and the rim is a poor predictor of clump properties (Section 3.2), as is association with YSOs or PMS stars (Section 3.3), and there is no correlation between the age of PMS stars and radial distance from NGC 602. Although some clusters of PMS stars along the rim appear marginally younger than PMS stars surrounding NGC 602 ($\sim$2 Myr versus 3 Myr), they are coincident with strong CO emission, and thus the high extinction in these regions could cause their ages to appear younger than they truly are (Section 3.3.2).

Our analysis of the now-resolved subparsec-scale clumps in N90 has revealed the sequential star formation history of the

region, and its evolution relative to the SMC Wing. This more complete census of the total molecular gas mass in the region allows for an improved estimate of SFE on both by-clump and regional scales. After correction for CO-dark molecular gas content, we find that star formation in N90 is not more efficient than star formation in similarly massive solar-metallicity, higher-density environments.

We consider N90 in the context of star formation in general in metal-poor environments. Despite the low-metallicity and low-density environment of the SMC Wing, the properties of molecular clumps and SFE in N90 do not appear to dramatically differ from their Galactic counterparts. If we extend this conclusion from the SMC to other nearby, small galaxies, it is likely that although star formation is initially sporadic in such environments, once regions have developed for a sufficient period of time, their behavior does not depart significantly from the process of star formation in higher-metallicity, higher-density regions.

Appendix
Clump and YSO Properties

We present tables of the properties of CO clumps (Table A1) and YSO candidates (Table A2) in N90.

Table A1
Clump Properties

ID	R.A. (°)	Decl. (°)	$^{12}CO_{pk}$ (K)	$^{13}CO_{pk}$ (K)	W_{12} (K km s^{-1})	R (pc)	$v_{LSRK, 12}$ (km s^{-1})	$\sigma_{v,12}$ (km s^{-1})	M_{LTE} ($M_\odot$)	$M_{X_{CO,B}}$ ($M_\odot$)	Σ ($M_\odot$ pc^{-2})	ρ_c ($M_\odot$ pc^{-3})	M_{vir} ($M_\odot$)	α_{vir}	Assoc. YSO	Group
1	22.3982	−73.5501	22.55	6.26	9355.61	0.55	171.88	0.90	245.1	188.9	201.7	1008.6	464.7	2.5		
2	22.3986	−73.5581	21.85	3.79	5146.64	0.62	173.74	0.56	102.6	103.9	86.8	434.2	203.1	2.0	Y270	r
3	22.3990	−73.5506	20.20	7.11	13901.61	0.61	173.55	0.93	286.1	280.7	243.4	1217.1	544.6	1.9	Y327	
4	22.3984	−73.5610	20.01	4.96	7215.35	0.50	174.96	1.07	163.6	145.7	183.7	918.7	603.0	4.1	Y251	r
5	22.4135	−73.5553	18.15	4.97	5699.55	0.58	171.30	0.61	143.6	115.1	109.1	545.3	227.7	2.0	Y312	
6	22.4002	−73.5647	16.54	4.24	4298.67	0.49	168.72	0.71	83.5	86.8	116.9	584.3	257.2	3.0	Y223	r
7	22.4208	−73.5583	16.41	2.66	3721.89	0.64	171.09	0.38	44.7	75.2	57.6	287.9	96.8	1.3		
8	22.4314	−73.5622	16.23	3.99	4976.71	0.68	166.36	0.48	61.9	100.5	68.4	341.8	166.7	1.7	Y287	
9	22.4001	−73.5644	16.22	3.69	3596.83	0.51	167.30	0.69	65.5	72.6	87.5	437.4	258.7	3.6		r
10	22.4369	−73.5573	15.37	4.71	5210.15	0.61	166.32	0.65	123.3	105.2	88.9	444.5	268.0	2.5	Y326	
11	22.4234	−73.5622	15.13	3.71	7338.28	0.76	166.79	0.56	153.5	148.2	81.8	409.1	251.7	1.7		
12	22.4053	−73.5649	14.72	1.86	7512.51	0.77	169.59	0.64	91.6	151.7	82.5	412.6	324.2	2.1	Y227, Y240	r
13	22.3320	−73.5535	14.42	2.79	7856.07	0.77	161.21	0.88	142.5	158.6	85.3	426.6	619.5	3.9	Y217	r
14	22.4049	−73.5643	14.19	2.26	3586.16	0.47	168.89	0.75	56.4	72.4	102.3	511.6	281.7	3.9		r
15	22.4336	−73.5621	13.88	2.41	1850.34	0.54	166.14	0.38	26.9	37.4	40.1	200.6	82.0	2.2		
16	22.3601	−73.5416	13.51	1.76	2758.22	0.51	167.72	0.59	64.0	55.7	67.9	339.5	186.1	3.3	A340	
17	22.4277	−73.5617	13.29	2.95	3921.42	0.52	166.55	0.59	82.5	79.2	93.6	467.9	190.3	2.4		
18	22.3456	−73.5475	13.23	3.63	4710.30	0.53	162.64	0.67	62.6	95.1	106.7	533.3	250.4	2.6	Y285	r
19	22.3787	−73.5684	13.07	2.92	3776.69	0.58	164.70	0.68	101.9	76.3	72.2	360.8	278.6	3.7	Y170	r
20	22.4189	−73.5547	12.43	1.48	2580.00	0.53	170.18	0.53	⋯	52.1	59.7	298.4	157.5	3.0		
21	22.3354	−73.5518	10.94	3.84	2631.43	0.42	162.40	0.92	78.2	53.1	95.3	476.3	369.6	7.0	Y237	r
22	22.3991	−73.5614	10.58	1.83	1345.89	0.37	177.47	0.54	34.8	27.2	64.3	321.4	112.9	4.2		r
23	22.4154	−73.5547	10.57	2.91	1717.81	0.44	171.33	0.62	26.4	34.7	56.8	283.8	178.0	5.1		
24	22.3575	−73.5798	10.07	2.68	1896.67	0.57	166.28	0.34	40.2	38.3	37.4	187.1	67.7	1.8	Y090	
25	22.4136	−73.5715	10.00	1.19	1000.70	0.38	167.03	0.47	⋯	20.2	44.0	220.0	88.9	4.4		
26	22.4104	−73.5646	9.92	1.35	1208.22	0.42	169.67	0.45	⋯	24.4	44.4	222.0	89.6	3.7		r
27	22.4007	−73.5723	9.88	1.70	774.79	0.40	168.02	0.38	12.7	15.6	31.0	155.2	59.7	3.8		
28	22.3326	−73.5521	9.77	1.85	2631.80	0.52	161.14	0.73	39.0	53.1	62.7	313.4	287.3	5.4		r
29	22.4189	−73.5569	9.74	1.19	740.74	0.40	171.20	0.33	⋯	15.0	29.6	148.2	45.2	3.0		
30	22.4168	−73.5546	9.73	1.78	1530.42	0.43	170.20	0.56	23.5	30.9	54.2	270.8	140.1	4.5		
31	22.3591	−73.5762	9.02	1.35	1653.76	0.40	165.93	0.69	⋯	33.4	66.9	334.5	198.7	6.0		
32	22.3323	−73.5563	9.02	1.25	1757.42	0.48	162.98	0.67	⋯	35.5	48.5	242.7	229.8	6.5	Y196	r
33	22.3817	−73.5694	8.74	2.81	892.46	0.36	171.44	0.58	28.9	18.0	43.2	216.2	130.1	7.2	Y162	r
34	22.4150	−73.5647	8.00	1.14	686.99	0.40	169.48	0.36	⋯	13.9	27.7	138.6	53.0	3.8		r
35	22.3977	−73.5684	7.91	1.51	732.43	0.38	170.33	0.45	⋯	14.8	32.3	161.7	81.3	5.5		r
36	22.3996	−73.5734	7.90	1.27	943.82	0.44	166.46	0.43	⋯	19.1	31.7	158.7	84.3	4.4		
37	22.3955	−73.5677	7.73	1.16	805.49	0.38	171.55	0.49	⋯	16.3	35.6	177.8	94.8	5.8		r
38	22.3849	−73.5691	7.55	3.35	1028.77	0.37	170.68	0.68	34.3	20.8	47.5	237.4	182.3	8.8	Y171	r
39	22.3970	−73.5643	7.37	1.38	842.36	0.42	166.68	0.53	⋯	17.0	30.5	152.7	123.8	7.3		r
40	22.3919	−73.5699	7.30	1.04	905.78	0.43	170.20	0.50	⋯	18.3	31.2	156.0	111.6	6.1	Y174	r
41	22.4052	−73.5700	7.26	1.38	697.39	0.41	170.67	0.45	⋯	14.1	26.1	130.7	87.5	6.2		
42	22.3303	−73.5558	7.00	1.55	1461.28	0.51	162.82	0.69	⋯	29.5	35.6	177.8	259.0	8.8	Y197	r
43	22.3272	−73.5565	6.98	1.23	934.29	0.42	163.04	0.57	⋯	18.9	33.3	166.5	144.1	7.6	Y179	r
44	22.4006	−73.5748	6.92	1.39	1363.03	0.62	166.89	0.67	⋯	27.5	22.5	112.7	289.2	10.5		
45	22.3971	−73.5735	6.89	1.15	1016.27	0.43	165.09	0.65	⋯	20.5	35.6	177.8	190.1	9.3	Y148	
46	22.3926	−73.5594	6.79	1.31	691.45	0.40	177.65	0.38	⋯	14.0	27.4	137.2	60.9	4.4		r
47	22.4063	−73.5663	6.74	1.38	1452.12	0.48	170.65	0.57	⋯	29.3	40.1	200.6	164.4	5.6		r

Table A1
(Continued)

ID	R.A. (°)	Decl. (°)	$^{12}CO_{pk}$ (K)	$^{13}CO_{pk}$ (K)	W_{12} (K km s^{-1})	R (pc)	$v_{LSRK,\,12}$ (km s^{-1})	$\sigma_{v,12}$ (km s^{-1})	M_{LTE} ($M_\odot$)	$M_{X_{CO,B}}$ ($M_\odot$)	Σ ($M_\odot$ pc^{-2})	ρ_c ($M_\odot$ pc^{-3})	M_{vir} ($M_\odot$)	α_{vir}	Assoc. YSO	Group
48	22.3403	−73.5440	6.72	1.55	1711.77	0.53	162.08	0.56	⋯	34.6	39.6	198.2	175.5	5.1		r
49	22.3350	−73.5548	6.70	1.53	832.18	0.37	164.05	0.61	⋯	16.8	38.8	193.9	146.9	8.7	Y206	r
50	22.3423	−73.5468	6.55	1.28	952.40	0.43	160.74	0.61	⋯	19.2	32.6	163.1	169.7	8.8		r
51	22.3896	−73.5740	6.42	1.12	614.31	0.41	162.82	0.44	⋯	12.4	23.7	118.3	81.4	6.6		
52	22.4097	−73.5641	6.11	1.19	460.36	0.35	168.86	0.46	⋯	9.3	23.7	118.3	77.3	8.3		r
53	22.3946	−73.5736	5.67	0.90	509.58	0.43	164.36	0.37	⋯	10.3	17.6	88.1	61.1	5.9		
54	22.4073	−73.5660	5.67	1.26	1443.38	0.42	168.87	0.73	⋯	29.1	52.8	264.2	232.7	8.0		r
55	22.4035	−73.5640	5.67	1.81	363.58	0.33	175.09	0.46	16.3	7.3	21.2	105.8	73.6	10.0		r
56	22.4025	−73.5727	5.65	1.20	559.86	0.40	168.54	0.49	⋯	11.3	22.4	111.8	99.0	8.8		
57	22.3349	−73.5460	5.60	1.08	528.11	0.39	161.49	0.45	⋯	10.7	21.8	108.9	84.7	7.9		r
58	22.4054	−73.5650	5.52	1.19	669.50	0.40	172.79	0.56	⋯	13.5	26.7	133.5	132.5	9.8		r
59	22.3391	−73.5456	5.48	1.03	353.19	0.34	160.94	0.37	⋯	7.1	19.3	96.7	48.8	6.8		r
60	22.4206	−73.5718	5.39	0.85	297.48	0.39	166.52	0.28	⋯	6.0	12.7	63.6	32.7	5.4		
61	22.3861	−73.5759	5.37	0.96	253.89	0.35	169.09	0.33	⋯	5.1	13.5	67.7	39.6	7.7		
62	22.4055	−73.5647	5.19	1.03	330.24	0.37	171.85	0.37	⋯	6.7	15.8	79.1	53.0	7.9		r
63	22.4037	−73.5653	5.19	1.06	943.70	0.43	166.95	0.64	⋯	19.1	32.7	163.4	186.7	9.8		r
64	22.3686	−73.5756	5.12	0.91	325.28	0.37	163.52	0.37	⋯	6.6	15.5	77.6	51.3	7.8		
65	22.4047	−73.5600	4.97	1.30	329.91	0.34	168.44	0.46	⋯	6.7	18.0	89.8	76.3	11.5	Y264	r
66	22.3406	−73.5466	4.77	1.08	464.89	0.45	161.06	0.43	⋯	9.4	14.8	73.9	85.9	9.1		r
67	22.3292	−73.5644	4.62	1.28	548.05	0.42	162.92	0.49	⋯	11.1	19.5	97.6	107.8	9.7		r
68	22.3265	−73.5572	4.41	1.39	740.07	0.42	162.90	0.67	⋯	14.9	27.1	135.5	195.5	13.1		r
69	22.3185	−73.5669	4.39	1.15	293.45	0.37	165.99	0.39	⋯	5.9	13.6	68.1	59.8	10.1		r
70	22.4111	−73.5636	4.31	1.36	217.83	0.32	165.19	0.40	⋯	4.4	13.7	68.7	54.7	12.4		r
71	22.4083	−73.5658	4.26	0.96	513.34	0.41	167.73	0.40	⋯	10.4	20.0	99.8	69.7	6.7		r
72	22.3363	−73.5683	4.22	1.15	464.06	0.43	162.36	0.53	⋯	9.4	16.4	82.1	126.3	13.5		
73	22.4065	−73.5619	4.20	0.81	194.54	0.31	179.52	0.30	⋯	3.9	12.7	63.4	30.5	7.8	Y255	r
74	22.4224	−73.5715	4.08	1.02	209.90	0.39	166.81	0.24	⋯	4.2	9.0	45.1	22.9	5.4		
75	22.3974	−73.5773	4.04	1.05	433.77	0.49	167.69	0.28	⋯	8.8	11.8	59.2	38.8	4.4		
76	22.3687	−73.5699	4.03	0.97	420.55	0.43	172.38	0.47	⋯	8.5	15.0	74.8	98.0	11.5	Y142	r
77	22.3818	−73.5721	3.99	1.10	215.29	0.35	171.62	0.36	⋯	4.3	11.5	57.5	47.8	11.0		
78	22.3841	−73.5757	3.98	1.65	139.30	0.30	164.30	0.29	⋯	2.8	9.6	48.2	26.7	9.5		
79	22.3734	−73.5751	3.93	1.35	179.92	0.32	170.87	0.34	⋯	3.6	11.4	56.9	38.1	10.5	Y118	
80	22.3435	−73.5457	3.82	1.29	196.62	0.33	160.71	0.34	⋯	4.0	11.4	57.0	41.3	10.4		r
81	22.3399	−73.5450	3.81	1.05	718.68	0.41	162.25	0.73	⋯	14.5	27.5	137.3	228.4	15.7		r
82	22.3666	−73.5751	3.76	1.04	180.02	0.36	165.65	0.32	⋯	3.6	8.9	44.4	38.8	10.7		
83	22.4257	−73.5635	3.74	1.10	151.55	0.33	169.65	0.38	⋯	3.1	8.7	43.7	50.4	16.5		
84	22.3195	−73.5611	3.66	0.86	206.17	0.36	162.19	0.40	⋯	4.2	10.1	50.3	59.8	14.4	Y143	r
85	22.4143	−73.5649	3.63	0.89	123.62	0.31	167.28	0.33	⋯	2.5	8.2	41.1	34.7	13.9		r
86	22.3300	−73.5549	3.56	1.24	322.38	0.40	162.55	0.42	⋯	6.5	12.9	64.7	72.9	11.2		r
87	22.3910	−73.5600	3.56	1.12	162.66	0.33	177.21	0.38	⋯	3.3	9.8	48.8	50.5	15.4		r
88	22.4038	−73.5721	3.54	0.75	164.01	0.31	168.88	0.33	⋯	3.3	10.8	54.1	35.5	10.7		
89	22.3265	−73.5649	3.47	1.03	184.61	0.33	162.45	0.41	⋯	3.7	11.1	55.3	57.8	15.5		r
90	22.4005	−73.5745	3.20	0.91	174.52	0.37	164.11	0.31	⋯	3.5	8.0	40.2	38.4	10.9		
91	22.3953	−73.5727	3.16	0.72	120.61	0.26	165.04	0.35	⋯	2.4	11.1	55.6	33.1	13.6		
92	22.3961	−73.5563	3.11	0.73	89.55	0.31	177.72	0.28	⋯	1.8	5.8	29.2	26.0	14.4		r
93	22.3255	−73.5644	3.07	1.26	308.87	0.38	163.82	0.50	⋯	6.2	13.8	68.8	99.6	16.0		r
94	22.3362	−73.5476	2.95	1.02	81.51	0.30	162.29	0.28	⋯	1.6	5.9	29.3	25.2	15.3		r

Table A1
(Continued)

ID	R.A. (°)	Decl. (°)	$^{12}CO_{pk}$ (K)	$^{13}CO_{pk}$ (K)	W_{12} (K km s^{-1})	R (pc)	$v_{LSRK, 12}$ (km s^{-1})	$\sigma_{v,12}$ (km s^{-1})	M_{LTE} ($M_\odot$)	$M_{X_{CO,B}}$ ($M_\odot$)	Σ ($M_\odot$ pc^{-2})	ρ_c ($M_\odot$ pc^{-3})	M_{vir} ($M_\odot$)	α_{vir}	Assoc. YSO	Group
95	22.3087	−73.5570	2.92	0.98	72.28	0.30	162.47	0.23	⋯	1.5	5.0	25.1	16.5	11.3		
96	22.3258	−73.5522	2.91	1.32	80.05	0.31	161.55	0.24	⋯	1.6	5.4	27.1	19.3	11.9		r
97	22.3906	−73.5716	2.90	0.87	83.71	0.31	163.52	0.25	⋯	1.7	5.6	27.9	20.5	12.1		
98	22.3394	−73.5430	2.81	0.52	123.97	0.35	160.78	0.30	⋯	2.5	6.5	32.4	33.1	13.2		r
99	22.4028	−73.5731	2.76	0.85	82.34	0.28	167.84	0.25	⋯	1.7	6.5	32.6	19.1	11.5		
100	22.3662	−73.5755	2.74	1.04	84.38	0.26	164.22	0.27	⋯	1.7	7.7	38.7	20.1	11.8		
101	22.3162	−73.5620	2.69	0.83	170.67	0.37	161.04	0.35	⋯	3.4	8.2	41.2	46.7	13.5		r
102	22.4179	−73.5538	2.68	0.82	94.77	0.28	171.81	0.32	⋯	1.9	7.8	39.0	29.4	15.3		
103	22.4082	−73.5589	2.65	1.22	98.20	0.28	168.46	0.38	⋯	2.0	7.9	39.7	43.2	21.8		r
104	22.3223	−73.5644	2.65	0.57	103.14	0.30	164.09	0.35	⋯	2.1	7.2	35.8	39.2	18.8		r
105	22.3216	−73.5625	2.58	0.98	396.29	0.47	162.03	0.51	⋯	8.0	11.7	58.3	127.9	16.0		r
106	22.3683	−73.5777	2.56	1.13	121.61	0.34	170.15	0.35	⋯	2.5	6.9	34.5	44.2	18.0		
107	22.3374	−73.5462	2.56	1.27	204.92	0.37	159.52	0.64	⋯	4.1	9.4	47.2	161.5	39.0		r
108	22.3201	−73.5615	2.50	1.04	93.63	0.35	160.73	0.28	⋯	1.9	4.9	24.6	28.6	15.1		r
109	22.3906	−73.5732	2.36	0.81	59.62	0.28	164.27	0.24	⋯	1.2	4.8	24.1	17.6	14.6		
110	22.3332	−73.5466	2.25	0.69	69.29	0.37	160.04	0.26	⋯	1.4	3.3	16.6	25.4	18.1		r

Note. Clumps without LTE mass estimates have ^{13}CO S/N < 3. ρ_c is the volume density at 0.1 pc. "Assoc. YSO" gives the first four characters of the identifiers assigned by Carlson et al. (2011) and listed in Table A2 of any YSOs that fall within the projected 2D boundaries of the clump. A denotation of "r" in Group indicates the clump is on the N90 rim. Error estimates for most quantities are available in a complete, machine-readable version of this table.

(This table is available in machine-readable form.)

Table A2
YSO Properties

ID	Name	R.A. (°)	Decl. (°)	M ($M_\odot$)	$\dot{M}$ ($10^{-6}\ M_\odot\ \mathrm{yr}^{-1}$)
Y090	J012925.97-733446.8	22.3582	−73.5797	3.71	35.58
Y096	J012906.41-733348.6	22.2767	−73.5635	7.78	3.50
Y118	J012929.62-733430.1	22.3734	−73.5750	2.00	0.36
Y142	J012928.56-733411.9	22.3690	−73.5700	3.54	1.93
Y143	J012916.77-733340.7	22.3199	−73.5613	2.02	0.19
Y148	J012935.11-733423.9	22.3963	−73.5733	3.64	7.48
Y149	J012856.16-733242.4	22.2340	−73.5451	2.93	0.33
Y162	J012931.68-733409.2	22.3820	−73.5692	2.91	91.79
Y163	J012859.33-733244.8	22.2472	−73.5458	2.89	0.43
Y170	J012930.90-733405.6	22.3788	−73.5682	3.33	11.20
Y171	J012932.39-733408.4	22.3850	−73.5690	3.28	6.61
Y174	J012934.05-733411.7	22.3919	−73.5699	3.58	0.94
Y179	J012918.44-733324.9	22.3269	−73.5569	2.24	4.22
Y196	J012919.88-733322.5	22.3328	−73.5563	3.76	0.75
Y197	J012918.95-733319.4	22.3290	−73.5554	3.57	1.18
Y198	J012936.38-733403.6	22.4016	−73.5677	5.94	6.05
Y206	J012920.48-733316.8	22.3353	−73.5547	2.88	1.75
Y217	J012919.87-733312.5	22.3328	−73.5535	3.88	1.40
Y223	J012935.89-733351.7	22.3996	−73.5644	3.93	34.07
Y227	J012937.37-733352.4	22.4057	−73.5646	6.99	0.38
Y237	J012920.64-733306.3	22.3360	−73.5518	4.14	3.56
Y240	J012937.99-733352.8	22.4083	−73.5647	6.17	4.24
Y251	J012935.64-733339.5	22.3985	−73.5610	3.50	16.98
Y255	J012937.60-733342.9	22.4067	−73.5619	3.23	4.28
Y264	J012936.99-733336.1	22.4041	−73.5600	3.20	0.29
A270	J012935.51-733330.3	22.3980	−73.5584	6.48	36.11
Y270i	J012935.51-733330.3	22.3980	−73.5584	6.16	251.03
Y271	J012933.43-733323.3	22.3893	−73.5565	2.32	0.68
Y283	J012930.20-733310.5	22.3759	−73.5529	2.23	0.76
Y285	J012923.06-733251.5	22.3461	−73.5476	2.92	0.07
Y287	J012943.36-733343.1	22.4307	−73.5620	3.19	0.24
Y288	J012942.42-733341.6	22.1768	−73.0120	3.58	32.66
Y290	J012937.08-733325.4	22.4045	−73.5570	3.50	0.08
Y312	J012939.17-733318.9	22.4132	−73.5553	3.31	0.39
Y326	J012944.75-733325.2	22.4365	−73.5570	2.79	2.51
Y327	J012935.69-733302.1	22.3987	−73.5506	6.45	2.27
Y340	J012926.56-733230.3	22.3607	−73.5418	2.33	0.17
A340	J012926.56-733230.3	22.3607	−73.5418	2.77	1.89
Y358	J012935.17-733242.5	22.3966	−73.5452	2.19	2.70
Y396	J012924.20-733152.8	22.3508	−73.5313	2.37	0.21
Y493	J012915.95-733017.6	22.3165	−73.5049	1.60	0.03
Y700	J013006.79-733258.9	22.5286	−73.5497	2.56	5.35
K340	J012926.56-733230.3	22.3607	−73.5418	3.53	0.03
U364	J012908.96-733129.5	22.2873	−73.5249	2.41	2.81
U703	J012911.03-733039.6	22.2961	−73.5110	1.21	0.02

Note. IDs are the same as given in Carlson et al. (2011).

(This table is available in machine-readable form.)

ORCID iDs

Theo J. O'Neill ⬤ https://orcid.org/0000-0003-4852-6485
Rémy Indebetouw ⬤ https://orcid.org/0000-0002-4663-6827
Karin Sandstrom ⬤ https://orcid.org/0000-0002-4378-8534
Alberto D. Bolatto ⬤ https://orcid.org/0000-0002-5480-5686
Katherine E. Jameson ⬤ https://orcid.org/0000-0001-7105-0994
Molly K. Finn ⬤ https://orcid.org/0000-0001-9338-2594
Margaret Meixner ⬤ https://orcid.org/0000-0002-0522-3743
Elena Sabbi ⬤ https://orcid.org/0000-0003-2954-7643
Marta Sewiło ⬤ https://orcid.org/0000-0003-2248-6032

References

Abdo, A. A., Ackermann, M., Ajello, M., et al. 2010, ApJ, 710, 133
Astropy Collaboration, Price-Whelan, A. M., Sipőcz, B. M., et al. 2018, AJ, 156, 123
Astropy Collaboration, Robitaille, T. P., Tollerud, E. J., et al. 2013, A&A, 558, A33
Bertoldi, F., & McKee, C. F. 1992, ApJ, 395, 140
Bolatto, A. D., Leroy, A. K., Rosolowsky, E., Walter, F., & Blitz, L. 2008, ApJ, 686, 948
Bolatto, A. D., Wolfire, M., & Leroy, A. K. 2013, ARA&A, 51, 207
Bourke, T. L., Garay, G., Lehtinen, K. K., et al. 1997, ApJ, 476, 781
Bradski, G. 2000, The OpenCV Library, Dr. Dobb's Journal of Software Tools, 120, https://www.proquest.com/docview/202684726

Bressan, A., Marigo, P., Girardi, L., et al. 2012, MNRAS, 427, 127
Carlson, L. R., Sabbi, E., Sirianni, M., et al. 2007, ApJL, 665, L109
Carlson, L. R., Sewiło, M., Meixner, M., et al. 2011, ApJ, 730, 78
Caselli, P., Benson, P. J., Myers, P. C., & Tafalla, M. 2002, ApJ, 572, 238
Caselli, P., & Myers, P. C. 1995, ApJ, 446, 665
Chen, H. H.-H., Offner, S. S. R., Pineda, J. E., et al. 2020, arXiv:2006.07325
Chen, H. H.-H., Pineda, J. E., Goodman, A. A., et al. 2019, ApJ, 877, 93
Chevance, M., Madden, S. C., Fischer, C., et al. 2020, MNRAS, 494, 5279
Cignoni, M., Sabbi, E., Nota, A., et al. 2009, AJ, 137, 3668
Da Rio, N., & Robberto, M. 2012, AJ, 144, 176
De Marchi, G., Beccari, G., & Panagia, N. 2013, ApJ, 775, 68
Dobbs, C. L. 2015, MNRAS, 447, 3390
Dolphin, A. 2016, DOLPHOT: Stellar photometry, Astrophysics Source Code
    Library, ascl:1608.013
Dolphin, A. E. 2000, PASP, 112, 1383
Elmegreen, B. G. 1989, ApJ, 338, 178
Elmegreen, B. G., & Scalo, J. 2004, ARA&A, 42, 211
Ester, M., Kriegel, H.-P., Sander, J., & Xu, X. 1996, in Proc. 2nd Int. Conf. on
    Knowledge Discovery and Data Mining, ed. E. Simoudis, J. Han, &
    U. Fayyad (Menlo Park, CA: AAAI Press), 226, https://dl.acm.org/doi/10.
    5555/3001460.3001507
Evans, C. J., Hainich, R., Oskinova, L. M., et al. 2012, ApJ, 753, 173
Fahrion, K., Cormier, D., Bigiel, F., et al. 2017, A&A, 599, A9
Field, G. B., Blackman, E. G., & Keto, E. R. 2011, MNRAS, 416, 710
Finn, M. K., Indebetouw, R., Johnson, K. E., et al. 2022, AJ, 164, 64
Fukui, Y., Habe, A., Inoue, T., Enokiya, R., & Tachihara, K. 2021, PASJ,
    73, S1
Fukui, Y., Ohno, T., Tsuge, K., Sano, H., & Tachihara, K. 2020, arXiv:2005.
    13750
Fulmer, L. M., Gallagher, J. S., III, Hamann, W.-R., Oskinova, L. M., &
    Ramachandran, V. 2020, A&A, 633, A164
Galametz, M., Madden, S., Galliano, F., et al. 2009, A&A, 508, 645
Garden, R. P., Hayashi, M., Gatley, I., Hasegawa, T., & Kaifu, N. 1991, ApJ,
    374, 540
Ginsburg, A., Koch, E., Robitaille, T., et al. 2019, radio-astro-tools/spectral-
    cube: v0.4.4, Zenodo doi:10.5281/zenodo.2573901
Glover, S. C. O., & Mac Low, M.-M. 2011, MNRAS, 412, 337
Gordon, K. D., Bot, C., Muller, E., et al. 2009, ApJ, 690, L76
Gordon, K. D., Clayton, G. C., Misselt, K. A., Landolt, A. U., & Wolff, M. J.
    2003, ApJ, 594, 279
Gordon, K. D., Engelbracht, C. W., Rieke, G. H., et al. 2008, ApJ, 682, 336
Gordon, K. D., Meixner, M., Meade, M., et al. 2011, AJ, 142, 102
Gordon, K. D., Roman-Duval, J., Bot, C., et al. 2014, ApJ, 797, 85
Gouliermis, D. A., Quanz, S. P., & Henning, T. 2007, ApJ, 665, 306
Gouliermis, D. A., Schmeja, S., Dolphin, A. E., et al. 2012, ApJ, 748, 64
Grenier, I. A., Casandjian, J.-M., & Terrier, R. 2005, Sci, 307, 1292
Gritschneder, M., Burkert, A., Naab, T., & Walch, S. 2010, ApJ, 723, 971
Gvaramadze, V. V., Kniazev, A. Y., Gallagher, J. S., et al. 2021, MNRAS,
    503, 3856
Haberl, F., Sturm, R., Filipović, M. D., Pietsch, W., & Crawford, E. J. 2012,
    A&A, 537, L1
Harris, C. R., Millman, K. J., van der Walt, S. J., et al. 2020, Natur, 585, 357
Hénault-Brunet, V., Oskinova, L. M., Guerrero, M. A., et al. 2012, MNRAS,
    420, L13
Henize, K. G. 1956, ApJS, 2, 315
Hermelo, I., Lisenfeld, U., Relaño, M., et al. 2013, A&A, 549, A70
Heyer, M., Krawczyk, C., Duval, J., & Jackson, J. M. 2009, ApJ, 699, 1092
Heyer, M. H., & Brunt, C. M. 2004, ApJL, 615, L45
Hilditch, R. W., Howarth, I. D., & Harries, T. J. 2005, MNRAS, 357, 304
Hodge, P. W. 1983, ApJ, 264, 470
Hughes, A., Meidt, S. E., Colombo, D., et al. 2013, ApJ, 779, 46
Hughes, A., Wong, T., Ott, J., et al. 2010, MNRAS, 406, 2065
Hunter, J. D. 2007, CSE, 9, 90
Hutchings, J. B., Thompson, I. B., Cartledge, S., & Pazder, J. 1991, AJ,
    101, 933
Ikeda, N., Kitamura, Y., & Sunada, K. 2009, ApJ, 691, 1560
Imara, N., & Faesi, C. M. 2019, ApJ, 876, 141
Indebetouw, R., Brogan, C., Chen, C.-H. R., et al. 2013, ApJ, 774, 73
Indebetouw, R., Wong, T., Chen, C.-H. R., et al. 2020, ApJ, 888, 56
Jameson, K. E., Bolatto, A. D., Leroy, A. K., et al. 2016, ApJ, 825, 12
Jameson, K. E., Bolatto, A. D., Wolfire, M., et al. 2018, ApJ, 853, 111
Kalari, V. M., Rubio, M., Saldaño, H. P., & Bolatto, A. D. 2020, MNRAS,
    499, 2534
Kauffmann, J., Pillai, T., & Goldsmith, P. F. 2013, ApJ, 779, 185
Kazandjian, M. V., Pelupessy, I., Meijerink, R., Israel, F. P., & Spaans, M.
    2016, A&A, 595, A125

Kennicutt, R. C., & Evans, N. J. 2012, ARA&A, 50, 531
Kepley, A. A., Leroy, A. K., Johnson, K. E., Sandstrom, K., & Chen, C. H. R.
    2016, ApJ, 828, 50
Kroupa, P. 2001, MNRAS, 322, 231
Krumholz, M. R. 2013, MNRAS, 436, 2747
Kurucz, R. L. 1993, SYNTHE Spectrum Synthesis Programs and Line Data
    (Cambridge, MA: Smithsonian Astrophysical Observatory)
Lada, C. J., Muench, A. A., Rathborne, J., Alves, J. F., & Lombardi, M. 2008,
    ApJ, 672, 410
Langer, W. D., Velusamy, T., Pineda, J. L., Willacy, K., & Goldsmith, P. F.
    2014, A&A, 561, A122
Larson, R. B. 1981, MNRAS, 194, 809
Lebouteiller, V., Cormier, D., Madden, S. C., et al. 2019, A&A, 632, A106
Lee, C., Leroy, A. K., Schnee, S., et al. 2015, MNRAS, 450, 2708
Lee, E. J., Chang, P., & Murray, N. 2015, ApJ, 800, 49
Lee, E. J., Miville-Deschênes, M.-A., & Murray, N. W. 2016, ApJ, 833, 229
Lee, J.-K., Rolleston, W. R. J., Dufton, P. L., & Ryans, R. S. I. 2005, A&A,
    429, 1025
Lee, M.-Y., Stanimirović, S., Douglas, K. A., et al. 2012, ApJ, 748, 75
Lehner, N., Howk, J. C., Keenan, F. P., & Smoker, J. V. 2008, ApJ, 678, 219
Leroy, A., Bolatto, A., Stanimirovic, S., et al. 2007, ApJ, 658, 1027
Lin, Y., Wyrowski, F., Liu, H. B., et al. 2022, A&A, 658, A128
MacLaren, I., Richardson, K. M., & Wolfendale, A. W. 1988, ApJ, 333, 821
Madden, S. C., Cormier, D., Hony, S., et al. 2020, A&A, 643, A141
Madden, S. C., Galliano, F., Jones, A. P., & Sauvage, M. 2006, A&A, 446, 877
Mangum, J. G., Ginsburg, A. G., Henkel, C., et al. 2019, ApJ, 871, 170
McKinney, W. 2010, in Proc. 9th Python in Science, ed. S. van derWalt &
    J. Millman, 56, https://conference.scipy.org/proceedings/scipy2010/
    mckinney.html
McMullin, J. P., Waters, B., Schiebel, D., Young, W., & Golap, K. 2007, in
    ASP Conf. Ser. 376, Astronomical Data Analysis Software and Systems
    XVI, ed. R. A. Shaw, F. Hill, & D. J. Bell (San Francisco, CA: ASP), 127
Meaburn, J. 1980, MNRAS, 192, 365
Meixner, M., Panuzzo, P., Roman-Duval, J., et al. 2013, AJ, 146, 62
Muraoka, K., Homma, A., Onishi, T., et al. 2017, ApJ, 844, 98
Myers, P. C., Hatchfield, H. P., & Battersby, C. 2022, ApJ, 929, 34
Naslim, N., Tokuda, K., Onishi, T., et al. 2018, ApJ, 853, 175
Nayak, O., Meixner, M., Fukui, Y., et al. 2018, ApJ, 854, 154
Nayak, O., Meixner, M., Indebetouw, R., et al. 2016, ApJ, 831, 32
Nigra, L., Gallagher, J. S., Smith, L. J., et al. 2008, PASP, 120, 972
Nikolić, S., Garay, G., Rubio, M., & Johansson, L. E. B. 2007, A&A, 471, 561
Ochsendorf, B. B., Meixner, M., Chastenet, J., Tielens, A. G. G. M., &
    Roman-Duval, J. 2016, ApJ, 832, 43
Ochsendorf, B. B., Meixner, M., Roman-Duval, J., Rahman, M., &
    Evans, N. J. 2017, ApJ, 841, 109
Oka, T., Hasegawa, T., Sato, F., et al. 2001, ApJ, 562, 348
O'Neill, T. J., Indebetouw, R., Bolatto, A. D., Madden, S. C., & Wong, T.
    2022, ApJ, 933, 179
Oskinova, L. M., Sun, W., Evans, C. J., et al. 2013, ApJ, 765, 73
pandasdevelopment team 2022, pandas-dev/pandas: Pandas, v1.5.0, Zenodo,
    doi:10.5281/zenodo.3509134
Pedregosa, F., Varoquaux, G., Gramfort, A., et al. 2011, J. Mach. Learn. Res., 12,
    2825, https://www.jmlr.org/papers/volume12/pedregosa11a/pedregosa
    11a.pdf
Pineda, J. L., Langer, W. D., Goldsmith, P. F., et al. 2017, ApJ, 839, 107
Pineda, J. L., Langer, W. D., Velusamy, T., & Goldsmith, P. F. 2013, A&A,
    554, A103
Pirogov, L. E. 2009, ARep, 53, 1127
Rahmah, N., & Sitanggang, I. S. 2016, in IOP Conf. Ser. 31: Earth
    Environmental Science, 012012
Ramachandran, V., Hamann, W.-R., Oskinova, L. M., et al. 2019, A&A,
    625, A104
Requena-Torres, M. A., Israel, F. P., Okada, Y., et al. 2016, A&A, 589, A28
Ridge, N. A., Francesco, J. D., Kirk, H., et al. 2006, AJ, 131, 2921
Robitaille, T. 2019, APLpy v2.0: The Astronomical Plotting Library in Python,
    v2.0, Zenodo doi:10.5281/zenodo.2567476
Robitaille, T., & Bressert, E. 2012, APLpy: Astronomical Plotting Library in
    Python, Astrophysics Source Code Library, ascl:1208.017
Robitaille, T., Rice, T., Beaumont, C., et al. 2019, astrodendro: Astronomical
    data dendrogram creator, Astrophysics Source Code Library, ascl:1907.016
Robitaille, T. P. 2017, A&A, 600, A11
Robitaille, T. P., Whitney, B. A., Indebetouw, R., Wood, K., & Denzmore, P.
    2006, ApJS, 167, 256
Rolleston, W. R. J., Dufton, P. L., McErlean, N. D., & Venn, K. A. 1999,
    A&A, 348, 728
Rubele, S., Girardi, L., Kerber, L., et al. 2015, MNRAS, 449, 639

Rubele, S., Pastorelli, G., Girardi, L., et al. 2018, MNRAS, 478, 5017
Russell, S. C., & Dopita, M. A. 1992, ApJ, 384, 508
Saigo, K., Onishi, T., Nayak, O., et al. 2017, ApJ, 835, 108
Sandstrom, K. M., Bolatto, A. D., Draine, B. T., Bot, C., & Stanimirović, S. 2010, ApJ, 715, 701
Schmalzl, M., Gouliermis, D. A., Dolphin, A. E., & Henning, T. 2008, ApJ, 681, 290
Schruba, A., Leroy, A. K., Kruijssen, J. M. D., et al. 2017, ApJ, 835, 278
Schruba, A., Leroy, A. K., Walter, F., et al. 2012, AJ, 143, 138
Schultz, G. V., & Wiemer, W. 1975, A&A, 43, 133
Seabold, S., & Perktold, J. 2010, in 9th Python in Science Conf. Statsmodels: Econometric and Statistical Modeling with Python, 92
Seale, J. P., Looney, L. W., Wong, T., et al. 2012, ApJ, 751, 42
Seale, J. P., Meixner, M., Sewiło, M., et al. 2014, AJ, 148, 124
Shetty, R., Beaumont, C. N., Burton, M. G., Kelly, B. C., & Klessen, R. S. 2012, MNRAS, 425, 720
Sidorin, V. 2017, Quickclump: Identify clumps within a 3D FITS Datacube, v1.0, Astrophysics Source Code Library, ascl:1704.006
Solomon, P. M., Rivolo, A. R., Barrett, J., & Yahil, A. 1987, ApJ, 319, 730
Staveley-Smith, L., Sault, R. J., Hatzidimitriou, D., Kesteven, M. J., & McConnell, D. 1997, MNRAS, 289, 225
Szűcs, L., Glover, S. C. O., & Klessen, R. S. 2016, MNRAS, 460, 82
Tatematsu, K., Umemoto, T., Kandori, R., & Sekimoto, Y. 2004, ApJ, 606, 333
Tchernyshyov, K., Meixner, M., Seale, J., et al. 2015, ApJ, 811, 78
Tognelli, E., Prada Moroni, P. G., & Degl'Innocenti, S. 2011, A&A, 533, A109
Valdivia-Mena, M. T., Rubio, M., Bolatto, A. D., Saldaño, H. P., & Verdugo, C. 2020, A&A, 641, A97
van der Tak, F. F. S., Black, J. H., Schöier, F. L., Jansen, D. J., & van Dishoeck, E. F. 2007, A&A, 468, 627
Velusamy, T., Langer, W. D., Pineda, J. L., et al. 2010, A&A, 521, L18
Virtanen, P., Gommers, R., Oliphant, T. E., et al. 2020, NatMe, 17, 261
Waskom, M. L. 2021, JOSS, 6, 3021
Welty, D. E., Xue, R., & Wong, T. 2012, ApJ, 745, 173
Westerlund, B. E. 1964, MNRAS, 127, 429
Williams, J. P., de Geus, E. J., & Blitz, L. 1994, ApJ, 428, 693
Wolfire, M. G., Hollenbach, D., & McKee, C. F. 2010, ApJ, 716, 1191
Wolfire, M. G., Hollenbach, D., McKee, C. F., Tielens, A. G. G. M., & Bakes, E. L. O. 1995, ApJ, 443, 152
Wong, T., Hughes, A., Tokuda, K., et al. 2017, ApJ, 850, 139
Wong, T., Hughes, A., Tokuda, K., et al. 2019, ApJ, 885, 50
Wong, T., Oudshoorn, L., Sofovich, E., et al. 2022, ApJ, 932, 47
Xu, D., Li, D., Yue, N., & Goldsmith, P. F. 2016, ApJ, 819, 22
Yonekura, Y., Dobashi, K., Mizuno, A., Ogawa, H., & Fukui, Y. 1997, ApJS, 110, 21